

Copyright Undertaking

This thesis is protected by copyright, with all rights reserved.

By reading and using the thesis, the reader understands and agrees to the following terms:

1. The reader will abide by the rules and legal ordinances governing copyright regarding the use of the thesis.
2. The reader will use the thesis for the purpose of research or private study only and not for distribution or further reproduction or any other purpose.
3. The reader agrees to indemnify and hold the University harmless from and against any loss, damage, cost, liability or expenses arising from copyright infringement or unauthorized usage.

If you have reasons to believe that any materials in this thesis are deemed not suitable to be distributed in this form, or a copyright owner having difficulty with the material being included in our database, please contact lbsys@polyu.edu.hk providing details. The Library will look into your claim and consider taking remedial action upon receipt of the written requests.

**PROCESSING, CHARACTERISATION AND
RELATED APPLICATION OF MAGNETRON
SPUTTERED ALUMINUM NITRIDE FILMS**

SUBMITTED BY

LEUNG TSZ TAO

A THESIS SUBMITTED IN PARTIAL FULFILLMENT
OF THE REQUIREMENTS FOR THE DEGREE OF
MASTER OF PHILOSOPHY IN PHYSICS

AT

THE DEPARTMENT OF APPLIED PHYSICS

THE HONG KONG POLYTECHNIC UNIVERSITY

SEPTEMBER, 2003



Pao Yue-kong Library
PolyU • Hong Kong

CERTIFICATE OF ORIGINALITY

I hereby declare that this thesis is my own work and that, to the best of my knowledge and belief, it reproduces no material previously published or written nor material which has been accepted for the award of my any other degree or diploma, except where due acknowledgement has been made in the text.

_____ (Signed)

LEUNG TSZ TAO (Name of student)



Abstract

Aluminum nitride (AlN) thin films with different crystallographic structures were fabricated by radio frequency reactive magnetron sputtering technique. The film structure was characterized, and their physical properties, including the piezoelectric, dielectric and mechanical properties, were measured. Two aspects of information were attained. First, we gained the knowledge of the deposition condition dependence of the film structure, from which one can be able to control the film structure by appropriate selection of the preparation parameters. The second, we gained the knowledge of the structure dependence of the film properties.

It was found that films of nearly amorphous (na-), polycrystalline (p-), texture (t-) and epitaxial (e-) structure can be obtained through appropriate settings of substrate temperature (T_s), RF power (P_w) and the selection of substrate material. Three substrate materials, i.e. Si(100), Pt(111)/Si(100) and single crystal $Al_2O_3(00\cdot1)$ were used in the study. All the deposition runs had a fixed target-to-substrate distance (D) of 10 cm, which was much larger than the mean free path (ρ) of the particles (≈ 1 cm) in the vacuum of 5 m Torr. Under such a large D/ρ ratio, the species collided frequently in the vacuum. T_s and P_w have the effects of affecting the thermal and kinetic energies of the species. The influences of T_s and P_w compensate mutually with



each other. Namely, the effects caused by the use of a low T_s can be compensated by the use of a higher P_w , or vice versa.

When a low T_s and a low P_w were used, the na-AlN structure was formed. This structure contains small and randomly oriented AlN grains. The formation of such a film structure was independent on the selection of the substrate material. The corresponding ranges of T_s and P_w were presented in a T_s - P_w diagram, and was denoted as the na-AlN region. The na-AlN structure was formed because at low T_s and P_w conditions, the species involved in the sputtering process were relatively immobile on the substrate surface. With the use of high T_s and P_w (denoted as the p-AlN region in the T_s - P_w diagram), p- film was formed which contained larger AlN crystallites. The orientation of the crystallites was relatively random. For further increase in T_s and P_w , t-AlN was formed if a Si(100) or a Pt(111)/Si(100) substrate was used. e-AlN film was formed if an $\text{Al}_2\text{O}_3(00\cdot1)$ substrate was used.

The piezoelectric coefficient d_{33} of AlN films was measured by a laser interferometer. The true d_{33} of a film was correction for the clamping effect by the substrate. d_{33} of a na-AlN film was determined to be 0.28 pm V^{-1} . This result suggests that even a highly disordered AlN film could have detectable piezoelectric response. The range of d_{33} of the p-AlN films was found to lie in a broader range of $1.38 - 6.2 \text{ pm V}^{-1}$. The d_{33} value of a t-AlN film was 5.5 pm V^{-1} , which was close to the upper bound of the d_{33} of the p-AlN films. The dielectric properties of some selected AlN films were measured. The dielectric constant was found to be in the range of 9 - 13 in the frequency range of 10 kHz - 1 MHz.



The hardnesses and elastic moduli of the AlN films deposited on Si(100) were investigated by nanoindentation method. Their values were found to vary with the film structure. A na-AlN film had the lowest hardness and elastic modulus, i.e. around 12 GPa and 170 – 190 GPa, respectively. With the increase in the level of crystallinity, the films became less porous, and both the hardness and elastic modulus increased to a higher level. For a p-AlN film, the hardness and elastic modulus increased to 15 GPa and 220 – 240 GPa, respectively. For a t-AlN film, the hardness and elastic modulus were found to reach 21 GPa and 240 – 250 GPa, respectively.



Acknowledgements

I would like to acknowledge Dr. C. W. Ong, my chief supervisor, for his invaluable advice and his close supervision in my study period.

I would like to express my thanks to Mr. S. F. Wong and my colleagues for their assistance and support.

Thanks are also due to Mr. M. N. Yeung of Materials Research Center and the staff of our department for their technical support.

This study was supported by the Center for Smart Materials of The Hong Kong Polytechnic University, and an internal grant of The Hong Kong Polytechnic University.



Acronyms

AFM	Atomic Force Microscopy
CVD	Chemical Vapour Deposition
FTIR	Fourier Transform Infrared
MBE	Molecular Beam Epitaxy
PFM	Piezoresponse Force Microscopy
PLD	Pulsed Laser Deposition
RF	Radio Frequency
RMS	Reactive Magnetron Sputtering
RT	Room Temperature
SAW	Surface Acoustic Wave
XRD	X-Ray Diffraction



Table of contents

Abstract.....	i
Acknowledgements.....	iv
Acronyms.....	v
Table of contents.....	vi
List of figures.....	ix
List of tables.....	xiv
Chapter 1 Introduction.....	1-1
1.1 General background.....	1-1
1.1.1 Structure of AlN.....	1-1
1.1.2 Growth Techniques of AlN Films.....	1-3
1.1.3 AlN Film Properties and Applications.....	1-8
1.2 Scope of this study.....	1-10
Chapter 2 Experimental Techniques.....	2-1
2.1 Sample Preparation.....	2-1
2.1.1 Film Fabrication.....	2-1
2.1.2 Top Electrode Fabrication.....	2-5



THE HONG KONG POLYTECHNIC UNIVERSITY

2.2	Characterization.....	2-9
2.2.1	Structural Characterization.....	2-9
2.2.1.1	Film Thickness Measurements.....	2-9
2.2.1.2	Fourier Transform Infrared Spectroscopy.....	2-11
2.2.1.3	X-Ray Diffraction.....	2-13
2.2.2	Piezoelectric Coefficient Measurements.....	2-18
2.2.3	Impedance Analysis.....	2-24
2.2.4	Mechanical Properties	2-25
Chapter 3	Preparation Condition Dependence of AlN Film Structure.....	3-1
3.1	Summary of AlN Sample Fabrication Parameters.....	3-1
3.2	Thickness and Coating Rate.....	3-3
3.3	Four Types of AlN Film Structures.....	3-7
3.3.1	Nearly Amorphous AlN Structure.....	3-7
3.3.2	Polycrystalline AlN Structure.....	3-10
3.3.3	Texture and Epitaxial AlN Structures.....	3-12
3.4	T_s and P_w Dependence of AlN Film Structure.....	3-19
3.4.1	T_s - P_w Diagram.....	3-20
3.4.2	Growth Mechanisms.....	3-24
3.5	Structural Information Revealed by IR Absorption.....	3-28
3.6	Oxygen Contamination.....	3-33



Chapter 4	Structure Dependence of the Properties of AlN Films....	4-1
4.1	Piezoelectric Properties.....	4-1
4.1.1	Comparison of Piezoelectric Signals Collected Using a Lock-in Amplifier and a Spectrum Analyzer.....	4-1
4.1.2	Uniformity of d_{33} Value.....	4-5
4.1.3	Correction of Clamping Effect.....	4-8
4.1.4	Structure Dependence of the Piezoelectric Effect of AlN Films.....	4-9
4.2	Dielectric Properties.....	4-19
4.3	Mechanical Properties.....	4-22
4.3.1	Indentation Depth Dependence of Hardness and Young' Modulus	4-22
4.3.2	Microstructure Dependence of H and E of AlN Films.....	4-24
Chapter 5	Conclusions.....	5-1
References.....		R-1



List of figures

	Page
Fig. 1.1(a) Side view of the wurtzite structure of AlN.	1-2
Fig. 1.1(b) Top view of the wurtzite structure of AlN.	1-2
Fig. 1.2 Side view of a magnetron sputtering head and target.	1-5
Fig. 2.1(a) Schematic diagram of the radio-frequency reactive magnetron sputtering system	2-3
Fig. 2.1(b) Schematic diagram of the interior arrangement of the system	2-3
Fig. 2.4 The flow chart of the photolithographic process.	2-6
Fig. 2.5 The photolithographic process for producing conducting electrodes on AlN films.	2-8
Fig. 2.6 Diagram showing the film thickness measurement by using a surface profiler.	2-10
Fig. 2.7 The basic configuration of a FTIR spectrometer.	2-12
Fig. 2.8 Schematic diagram of the principle of X-ray diffraction.	2-14
Fig. 2.10 Schematic diagram of glancing incident x-ray diffraction	2-16
Fig. 2.11 Schematic diagram showing the set up for the observation of pole figure.	2-17



Fig. 2.12	Schematic diagram of a piezoelectric measurement.	2-18
Fig. 2.13	Schematic diagrams showing the clamping effect of a film for the measurement of d_{33} .	2-20
Fig. 2.14	Schematic diagram of the single beam laser interferometer for the measurements of piezoelectric coefficient.	2-22
Fig. 2.15	The equivalent circuit of an AlN film.	2-24
Fig. 2.16	A schematic presentation nanoindenter test.	2-26
Fig. 2.17	Typical load-unload curves obtained in a nano-indentation experiment.	2-28
Fig. 3.2(a)	Coating rate of AlN films as a function of sputtering pressure.	3-5
Fig. 3.2(b)	Coating rate of AlN films as a function of P_w .	3-5
Fig. 3.2(c)	Coating rate of AlN films as a function of T_s .	3-5
Fig. 3.3	Typical XRD 2θ - θ spectra and GIXD spectra (glancing angle = 3°) of na-AlN films deposited on the three different substrate materials, at $T_s = 100^\circ\text{C}$ and $P_w = 250$ W.	3-9
Fig. 3.4	Typical 2θ - θ scan spectra of p-AlN films deposited on three different substrate materials.	3-11
Fig. 3.5	Typical 2θ - θ spectra of t-AlN films deposited on Si(100) and Pt(111)/Si(100) substrates.	3-13
Fig. 3.6	Typical 2θ - θ spectra of e-AlN films deposited on $\text{Al}_2\text{O}_3(00\cdot1)$ substrate.	3-14
Fig. 3.7(a)	The schematic diagrams of the t-AlN structures.	3-12
Fig. 3.7(b)	The schematic diagrams of the e-AlN structures.	3-12



Fig. 3.8	Top view of the epitaxial relation between AlN(00·1) and Al ₂ O ₃ (00·1).	3-16
Fig. 3.9(a)	Pole figure of a t-AlN film deposited on Pt(111)/Si(100) substrates.	3-17
Fig. 3.9(b)	Pole figure an e-AlN film deposited on Al ₂ O ₃ (00·1) substrates.	3-17
Fig. 3.10	ϕ -scan of an e-AlN film deposited on Al ₂ O ₃ (00·1) substrates.	3-18
Fig. 3.11(a)	T _s -P _w diagrams of AlN films deposited on Si(100) substrates.	3-21
Fig. 3.11(b)	T _s -P _w diagrams of AlN films deposited on Pt(111)/Si(100) substrates.	3-21
Fig. 3.11(c)	T _s -P _w diagrams of AlN films deposited on Al ₂ O ₃ (00·1) substrates.	3-21
Fig. 3.12	Typical IR absorption spectra of na-AlN, p-AlN and t-AlN films deposited on Si(100) substrates.	3-29
Fig. 3.13(a)	Schematic diagram showing the generation of E ₁ (TO) mode of an AlN film in an IR absorption experiment.	3-31
Fig. 3.13(b)	Schematic diagram showing the generation of A ₁ (TO) mode of an AlN film in an IR absorption experiment.	3-31
Fig. 4.1	The displacement of the piezoelectric effect of AlN film as a function of applied voltage measured by a lock-in amplifier and a spectrum analyzer.	4-3
Fig. 4.2	Displacement vs. applied voltage measured at different positions on an AlN film.	4-5
Fig. 4.3(a)	The piezoelectric responses of an AlN film displayed by a spectrum analyzer with a input voltage at frequencies of 10 kHz.	4-7



Fig. 4.3(b)	The piezoelectric responses of an AlN film displayed by a spectrum analyzer with a input voltage at frequencies of 15 kHz.	4-7
Fig. 4.5	A plot of displacement vs. applied voltage for a na-AlN film (AlN#44).	4-11
Fig. 4.6(a)	Plots of displacement vs. applied voltage for a p-AlN film (AlN#32).	4-14
Fig. 4.6(b)	Plots of displacement vs. applied voltage for a p-AlN film (AlN#34).	4-14
Fig. 4.7	Surface displacement of AlN#40 as a function of applied voltage.	4-15
Fig. 4.8	Surface displacement for sample AlN#57 as a function of the applied voltage.	4-17
Fig. 4.9	d_{33} values of AlN films with different structures.	4-18
Fig. 4.10	Capacitance of AlN films in the frequency range of 10 kHz – 1 MHz.	4-19
Fig. 4.11(a)	Dielectric constants of AlN films in the frequency range of 10 kHz – 1MHz.	4-21
Fig. 4.11(b)	Tangent loss of AlN films in the frequency range of 10 kHz – 1MHz.	4-21
Fig. 4.12	Typical nanoindentation results hardness (H) and young's modulus (E) as functions of penetration depth.	4-23
Fig. 4.13(a)	The load-unload curve of AlN films with the structure of nearly amorphous.	4-25
Fig. 4.13(b)	The load-unload curve of AlN films with the structure of polycrystalline.	4-25
Fig. 4.13(c)	The load-unload curve of AlN films with the structure of texture.	4-25



Fig. 4.14	Hardness (H) and young's modulus (E) of AlN films having different film structures.	4-28
-----------	---	------



List of tables

	Page
Table 2.2	Preparation conditions of AlN films. 2-4
Table 2.3	The deposition condition of Au top electrode. 2-5
Table 2.9	d space of three major AlN lattice planes. 2-15
Table 2.18	The settings of maximum loads for the six nano-indentation experiments. 2-29
Table 3.1	Deposition conditions, thickness and coating rate of AlN films. 3-2
Table 3.14	AlN optical phonon frequencies at different modes. 3-32
Table 4.4	The deposition conditions and thickness of AlN films with different structures for piezoelectric measurements. 4-9
Table 4.14	Hardness (H) and elastic modulus (E) of AlN films having different film structures. 4-27



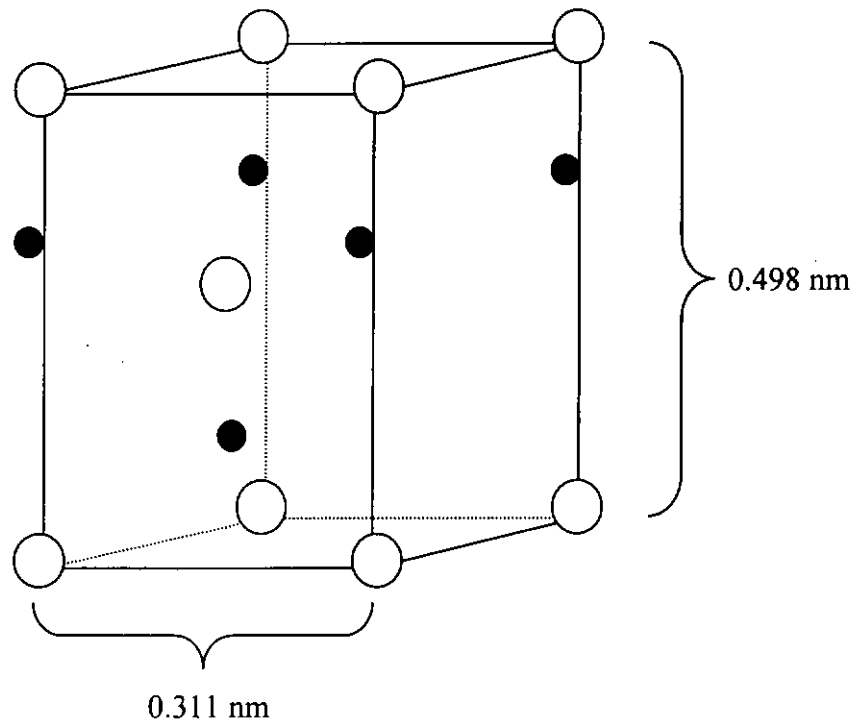
Chapter 1

Introduction

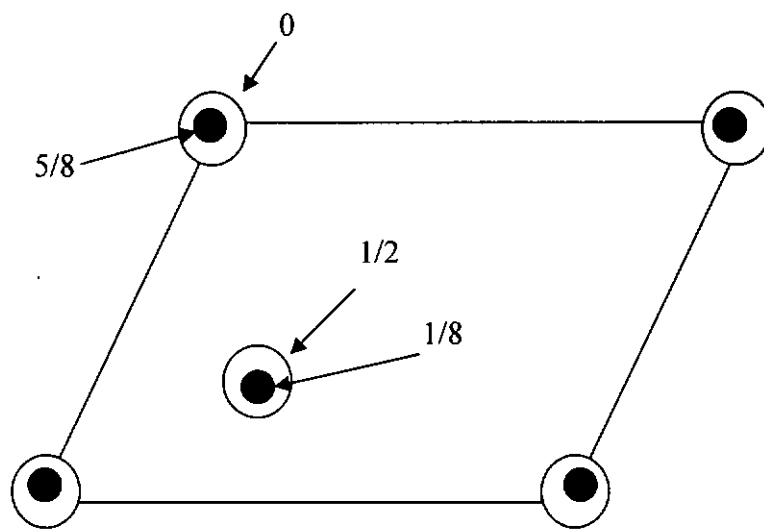
1.1 General background

1.1.1 Structure of AlN

Aluminum nitride (AlN) is a III-V nitride having a wurtzite hexagonal structure as shown in Fig.1.1. The lattice has lattice constants of $a = 3.11 \text{ \AA}$, $c = 4.98 \text{ \AA}$ [Kamiya, 1996]. Nowadays, AlN has attracted both scientific and application interests due to many novel properties of this material. AlN has a high electrical resistivity due to its large bandgap ($E_g \approx 6.28 \text{ eV}$). It also has a high dielectric strength. AlN is known to be a hard material having a hardness of 18 GPa [Watanabe, 1999]. In addition, AlN is a well-known piezoelectric material with a piezoelectric coefficient d_{33} of $4\text{-}5 \text{ pm V}^{-1}$ [Tsubouchi, 1981; Ruffner, 1999]. Having a high acoustic wave velocity, AlN is applied to make devices for the applications in telecommunications, such as microwave filters and resonators [Dubois, 1999]. Actually, AlN is more superior to other piezoelectric materials like zinc oxide (ZnO) and lead zirconate titanate (PZT) for having better acoustic properties, and so is selected to be studied in this project. Indeed, AlN has a fast surface acoustic wave (SAW) velocity of 6000 cm^{-1} . Therefore, surface acoustic wave filters made of AlN piezoelectric thin films are of great potential for the applications in mobile telecommunications.



(a)



(b)

Figure 1.1 The wurtzite structure of AlN. (a) Side view, and (b) top view: elevations of atoms from the base plane are in units of cell height.



1.1.2 Growth techniques of AlN films

The control of the microstructure and crystal orientation in the growth of AlN films is of particular interest because of their importance in some applications. For example, an AlN film with preferential c-axis orientation perpendicular to the substrate and a thickness of about 1 μm exhibits a resonance frequency higher than 2 GHz [Dubois, 1999; Lakin, 1995]. Such a film can be used to produce high frequency electronic filter in new generation mobile telecommunication system.

Many film fabrication techniques have been used to fabricate AlN films, and some of them are able to control effectively the microstructure and crystal orientation of AlN films by varying the preparation parameters. For example, pulsed laser deposition (PLD) is successful in preparing AlN films. However, its disadvantage is that the laser energy is very high, and when it is focused on the target (e.g. Al), Al particulates are generated which do not react fast enough with the ambient nitrogen. Consequently, stoichiometric AlN phase is not formed. Therefore, all successful cases of AlN film deposition by PLD were conducted with the use of AlN compound targets [Jagannadham, 1998; Vispute, 1994].

Chemical vapour deposition (CVD) is another important technique with good controllability of the microstructure and crystal orientation of AlN films. For example, Kung *et al* [Kung, 1995] and Chubachi *et al* [Chubachi, 1984] fabricated CVD AlN films by using trimethylaluminum, ammonia and hydrogen as the reactant gases. The substrate temperature was risen to above 1000°C. The film showed good crystallinity



and high quality. However, a general drawback of CVD technique is the necessity of using hazardous gases, which when being released to atmosphere would cause certain degree of pollution of environment.

Molecular beam epitaxy (MBE) is another technique which gives orderly preferential orientation of AlN films at high substrate temperature. Stevens *et al* [Stevens, 1994] revealed that AlN films deposited at higher substrate temperatures possessed better crystallinity. The full width half maximum (FWHM) of x-ray diffraction peak obtained from an omega scan was 0.7 deg for a film deposited at 900°C which was narrower than those of the films deposited at lower substrate temperatures. The major drawback of MBE is its low coating rate. Stevens mentioned that the coating rate of a MBE process was 70 nm/hr, which was too slow for commercial production.

Nowadays, both direct-current (dc) and radio-frequency (rf) reactive magnetron sputtering (RMS) are most widely used for mass production in industries. The high stability, good uniformity and good controllability are the advantages of RMS techniques. Furthermore, the highly c-axis orientated AlN films can be produced by using a low-cost metal Al target. The substrate temperature can be relatively low. Okano *et al* [Okano, 1992] revealed that AlN films with acceptable crystallinity could be obtained at substrate temperature as low as 300°C (a temperature due to the heating of plasma). And even lower substrate temperature of 100°C for successful deposition of AlN films was reported by Iriarte *et al* [Iriarte, 2002].



In a reactive sputtering process by using a magnetron gun, a magnet array is located on the back side of a sputtering target (Fig 1.2). The magnetic field serves to confine the plasma on the target surface. The energetic particles are accelerated to bombard and sputter the target surface.

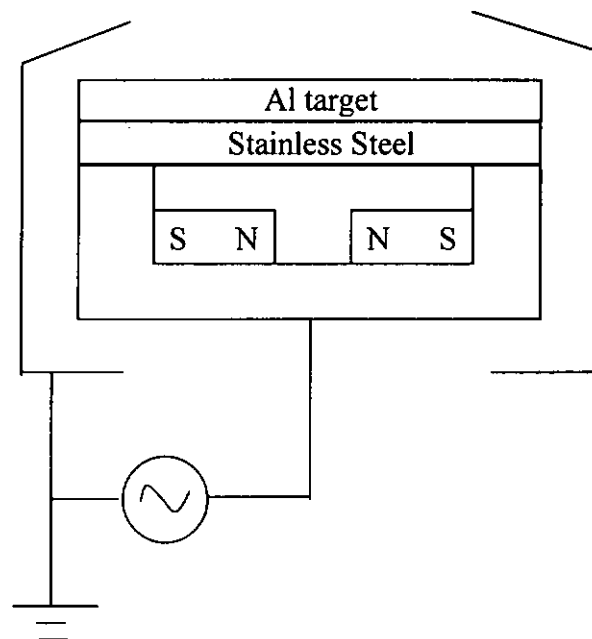
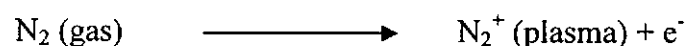
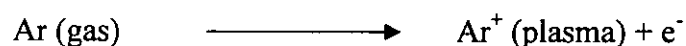


Fig. 1.2 Side view of a magnetron sputtering head and target.



Admixture of Ar and N₂ is chosen to be the sputtering gas. Ar is an inert gas and does not react with the target material. It is a relative heavy element and so facilitates transferring momentum to the target atoms. N₂ gas is mixed with Ar gas. The mixture is admitted into the chamber. When RF power is applied to the sputtering gun, the species are ionized to induce reactions like:



The Ar⁺ and N₂⁺ ions are then accelerated to bombard the Al target. The N₂⁺ ions may react with the Al atoms at the target surface. N- and Al-containing species are thus generated and deposited on the substrate. It should be noted that many authors claim that Al is much readily to react with oxygen (O) compared with nitrogen, because the bond energy of Al-O is higher than that of Al-N. The O atoms may come from some residual O-containing species in the vacuum chamber. This causes additional uncertainty and instability of the composition and quality of the deposits. Results show that although the ultimate pressure of our chamber is in the high vacuum range ($\approx 3 \times 10^{-6}$ Torr), the oxygen contamination is not observed in our films.



Reactive magnetron sputtering (RMS) is one of the most widely used deposition techniques in industries for quite a long time. It is shown to be successful in preparing texture/epitaxial AlN films with (00·1) preferential orientation along the normal of the substrate. Such a preferred orientation is desired for AlN films to be used in many devices. Loebel *et al* [Loebel, 2003] revealed that AlN films with good electromechanical coupling coefficient (k_t) and low dielectric loss could be attained if preferential c-axis orientation along the substrate normal is formed. In order to obtain AlN films of such a desired structure, many experiments have been done to investigate how the film structure depends on the preparation conditions. Results show that many parameters can affect the crystallographic structure of RMS AlN films. First, Loebel *et al* pointed out that the structure of substrates could strongly affect the preferential grain orientation of an AlN films due to lattice matching. Cheng *et al* [Cheng, 2003] reported that preferred (00·1) orientation of AlN films was enhanced with the decrease in the sputtering gas pressure. Assouar *et al* [Assouar, 2002] claimed that the concentration of nitrogen in the sputtering gases affected the formation of textured (00·1) orientation. This simple review shows that the results of the preparation condition dependence of the structure of RMS AlN films reported by different authors are apparently not consistent. One mission of this study is to reveal some possible growth mechanisms governing the structure of AlN films, so as to reconcile the results reported by the different authors.



1.1.3 AlN film properties and applications

AlN is a well-known piezoelectric material. When a voltage is applied to a piezoelectric AlN film, a mechanical strain is produced. This property is characterized by a piezoelectric coefficient (d) with a relationship of:

$$x = dV$$

where x is the displacement and V is the applied voltage. A larger value of d corresponds to a larger displacement induced by a certain applied voltage.

For an anisotropic piezoelectric material like AlN, the piezoelectric coefficients are presented in a tensor form denoted by d_{ij} . The first subscript refers to the direction of electric field applied to the material. The second subscript refers to the direction of the strain induced. Generally, the direction along the film thickness is denoted as the z -direction, and is labeled by $i = j = 3$. With this convention, the piezoelectric coefficient d_{33} is a measure of the displacement along z -direction responding to an electric field applied along the same direction.



Actually, the crystallographic structure of AlN films is expected to affect the piezoelectric coefficient significantly. To date, the correlation between the crystallographic structure and piezoelectric effect of AlN films is seldom reported. Most of the piezoelectric measurements on AlN films were carried out on samples having preferential orientation with the c-axis (00·1) along normal of the film [Lueng, 2000]. One exception is the study reported by Ruffner *et al* [Ruffner, 1999], who claimed that the piezoelectric coefficient of AlN films did not depend on the grain orientation. Therefore, it is of interest to know how the piezoelectric properties of AlN films would depend on the crystallographic structure, and is one of the topics to be investigated in the present study.

In the aspect of application, there is a great requirement of smaller sized band pass filters operating at higher frequency range (3 GHz) for mobile communication applications. AlN, ZnO and PZT are potential candidates for making this type of devices by utilizing their piezoelectric properties. In particular, they are more and more widely used in the fabrication of surface acoustic wave (SAW) filters [Kobayashi, 1995] — critical devices in telecommunication systems.



1.2 Scope of this study

The purpose of this study is to investigate how the magnitudes of substrate temperature (T_s) and RF power (P_w) and the selection of substrate materials affect the crystal structure and properties of RMS AlN films. In particular, three substrate materials were used. They were Si(100), Pt(111)/Si(100) and $\text{Al}_2\text{O}_3(00\cdot1)$. The results are discussed and compared with those reported in the literature. We found that there are very few papers published to report the preparation parameter dependence of the crystallographic structure of AlN films. Among these reports, Lee *et al* [Lee, 1995] only revealed the influence of sputtering pressure on the structure of AlN films, and Kusaka *et al* [Kusaka, 2002] reported the effect of sputtering gas pressure and nitrogen concentration (sputtering gases ratio) on the crystal orientation of AlN films.

In the first part of this study, AlN films were fabricated with different substrate temperatures, RF powers and substrate materials in order to produce samples of different structures. Other parameters, such as the substrate-to-target ratio and sputtering gas ratio were fixed. The structure and properties of these films were investigated. AlN films deposited on Si(100) were used for the infrared absorption (IR) measurements. X-ray diffraction (XRD) was employed to identify the crystallographic structure of the films.

The second part of this study is to measure the properties (electrical and mechanical) of the AlN films as functions of their crystallographic structure, so as to establish a correlation between the film structures and their physical properties.



Chapter 2

Experimental Techniques

2.1 Sample Preparation

2.1.1. Film fabrication

In this project, aluminium nitride (AlN) thin films were prepared by radio-frequency (RF) reactive magnetron sputtering technique. Schematic diagrams of the RF reactive magnetron sputtering system and the configuration of the vacuum chamber used for the deposition are shown in Fig. 2.1(a) and 2.1(b), respectively. The vacuum chamber is connected to a diffusion pump (without a liquid nitrogen cold trap), which is backed by a mechanical pump. A capacitive pressure transducer (MKS 122A Baratron gauge) and a hot cathode ionization gauge (ZJ-2 Guoguang) are used to measure the pressure inside the working chamber at rough vacuum range (> 1 mTorr) and high vacuum range (< 1 mTorr), respectively.

As shown in Fig. 2.1b, the substrate holder is mounted at the top flange of the chamber. The substrate holder is rotated to ensure the uniformity of the deposits. For the deposition of each batch of samples, three different substrate materials were used. They were Si(100) with electrical resistivity in the range of 15-25 Ω cm, platinum coated silicon denoted by Pt(111)/Si(100), and single crystal sapphire with the (00·1) planes in parallel to the surface, as denoted by Al₂O₃(00·1). Samples on the Si (100)



substrates were used for Fourier Transform infrared absorption (FTIR) measurements. The normal of the target makes an angle of 40° with the normal of substrate. The substrate-to-target distance (D) was set to be around 10 cm. We note that this distance is much larger than the mean free path (ρ) of the sputtering species, i.e. $\rho = \frac{5}{\text{pressure(mTorr)}} \text{ (in cm)} = 1 \text{ cm}$ [Iriarte, 2002]. The sputtering target is a metal Al disc (ϕ 2" in diameter, 3 mm thick and purity 99.999%). The sputter gas is a mixture of argon (Ar) and nitrogen (N_2), which is admitted into the chamber after the chamber is evacuated to the ultimate pressure of $\approx 2 \times 10^{-6}$ Torr. The flow rates (sccm) of Ar and N_2 are controlled automatically by using two mass flow controllers (MKS, Model 1259).

Before deposition, substrates were immersed in acetone and ethanol, and first degreased in an ultrasonic bath. The substrates were then blown with compressed air and loaded into the chamber. The chamber was pumped down to a base pressure of 4×10^{-6} Torr. The shutter in front of the target was first closed. Ar gas was then admitted into the chamber to build up a pressure of 200 mTorr. RF power (P_w) of 200 W was used to power the sputter head for pre-cleaning the target surface for 10 minutes. Admixture of Ar and N_2 in a molar ratio of 2 : 8 was then admitted into the chamber to build up an ambient pressure of 5 mTorr. The substrate was heated up to a preset temperature (T_s). The shutter was then opened to start deposition. Each deposition run lasted for 90 minutes. As summarized in Table 2.2, T_s was varied in the range from room temperature to 700°C , and P_w from 100 to 250 W.

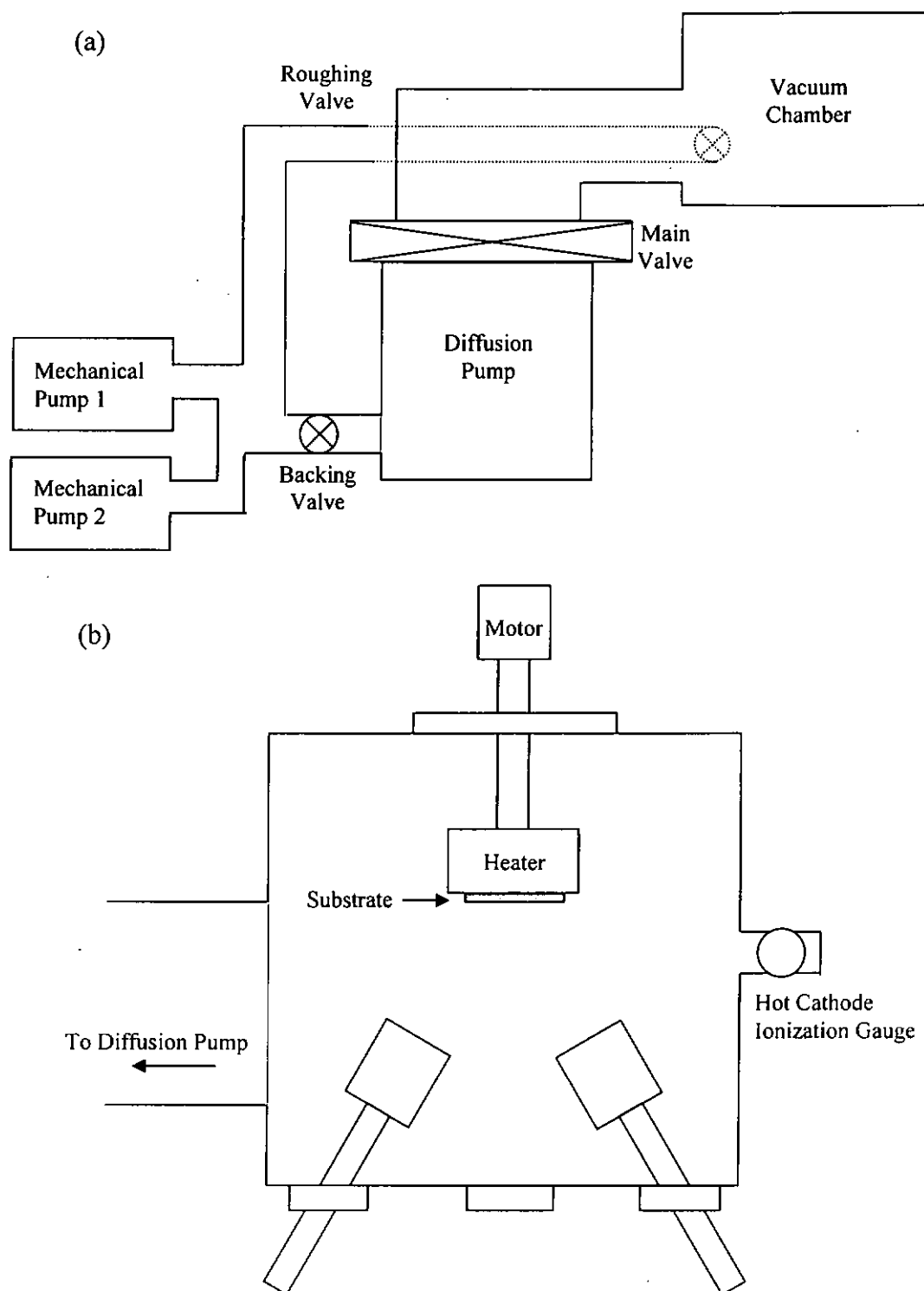


Fig. 2.1 (a) Schematic diagram of the radio-frequency reactive magnetron sputtering system, and (b) the interior arrangement of the system.



Target	Al disc (ϕ 2", 3 mm thick and purity 99.999%)
Substrate Temperature (T_s)	Room temperature – 700°C
RF Power (P_w)	100 – 250 W
Ambient pressure	5 mTorr
Ar/N ₂ gases ratio	2:8 (sccm), purity 99.995%
Target-to-substrate distance (D)	10 cm
Substrate	Si(100), Pt(111)/Si(100), Al ₂ O ₃ (00·1)

Table. 2.2 Preparation conditions of AlN films.



2.1.2. Top electrode fabrication

Metal electrodes were made on the film surface for electrical properties measurements. The electrode was made by sputtering a thin layer of gold (Au) film on the top surface of the film by using conditions listed in Table 2.3.

Trail was made by depositing an aluminum (Al) film on top to serve as the electrode (at $T_s = 200^\circ\text{C}$), but the Al film was found to react very quickly with the AlN film.

Temperature	200°C
Time	15 min.
Sputtering gas	Ar (10 sccm)
Sputtering pressure	35 mTorr
RF power	80 W
Thickness	200 – 300 nm

Table 2.3 The deposition condition of Au top electrode.

The photolithographic process was then carried out to make a pattern of the electrodes. The process was done in a clean room. Contamination of the AlN films can thus be minimized. The flow chart of the photolithographic process is shown in Fig. 2.4.

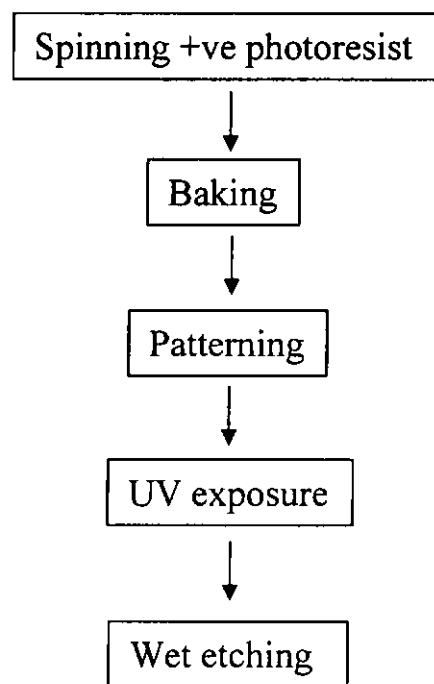


Fig 2.4 The flow chart of the photolithographic process.



The AlN films coated with Au top electrode was first spun with a layer of positive (+ve) photoresist (AZ3100, Clariant (China) Ltd) by a spin coater. The spinning speed was normally kept at 4500 rpm for 60 seconds. Then, the sample was put into a furnace and baked for 10 minutes at 80°C in order to remove the solvent and water vapour inside the +ve photoresist. An aligner was used to pattern the SAW device by covering the mask on the sample. UV light was directed to shine on the sample for 20 seconds. The exposed +ve photoresist was removed by a developer AZ300, [supplied by Clariant (China) Ltd]. The chemical solution consisting of KI, I₂ and H₂O was used to etch the exposed Au, and the pattern was produced. After removing the unexposed +ve photoresist by acetone and oxygen plasma, the patterning of the electrodes was completed. The photolithographic process for producing the electrodes is shown in Fig. 2.5. The control of etching time is a key factor for the success of producing a good pattern.

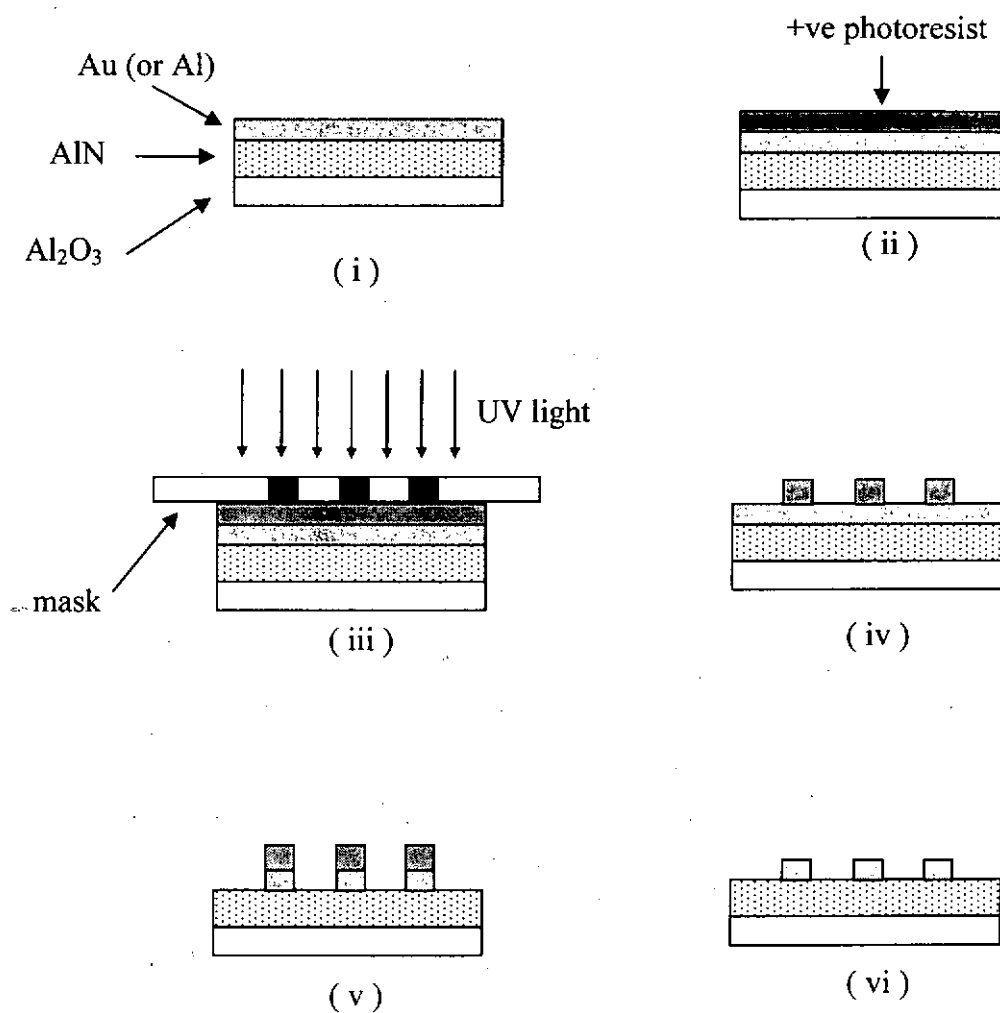


Fig. 2.5 The photolithographic process for producing conducting electrodes on AlN films.



2.2. Characterization

In this section, the experiment technique used for the structural characterization, and the measurements of the physical properties of the AlN films are described.

2.2.1. Structural Characterization

2.2.1.1 *Film thickness measurements*

The film thickness of all AlN samples was measured by using an α -Step surface profiler (KLA-Tencor P-10) which had a resolution of 1 nm. This system is used to measure the height of a small step, which is not more than 3 μm . By moving the stylus horizontally, the stylus experiences a sudden drop (or rise) at the edge (Fig. 2.6) such that an electrical signal is generated and detected. The displacement is determined via some calibration process. Of course, the applied load of the stylus should be extremely low in order to prevent from damaging the original film surface.

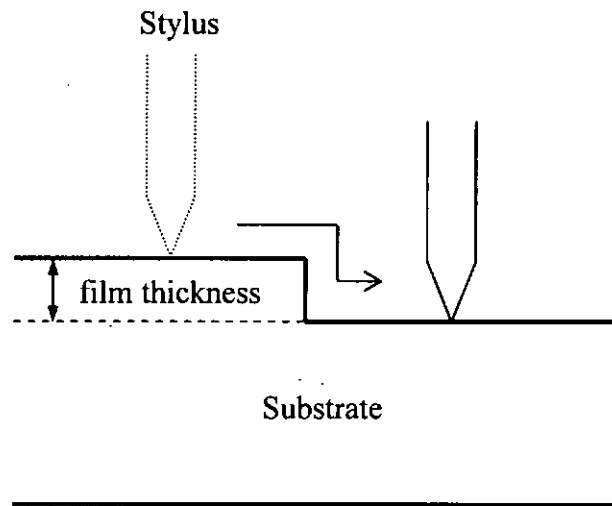


Fig. 2.6 Diagram showing the film thickness measurement by using a surface profiler.



2.2.1.2 Fourier Transform Infrared Spectroscopy

Fourier transform infrared absorption (FTIR) of the films was recorded by using a Nicolet's Magna-TRTM System (Model 750 FTIR) to analyze the chemical bonding formed in the films. The IR absorption spectra of the films in the wavenumber range of 400 – 4000 cm⁻¹ were recorded. The basic configuration of the FTIR spectrometer is shown Fig. 2.7. When the IR light source is incident to the beam splitter, the light source is split into two beams. One beam is reflected by a fixed mirror and other is reflected by a movable mirror. When the movable mirror moves back and front, the two beams interfere constructively or destructively. Consequently, the detector measures the variation of the intensity of the IR beam reflected from the stationary mirror. The IR absorption of the sample at different wavelengths can then be derived.

When the frequency of the incident infrared radiation is matched with resonance frequency of a vibrational mode of a chemical bond, the radiation will be strongly absorbed. The position of the absorption band can be used to identify the presence of a certain type of chemical bond.

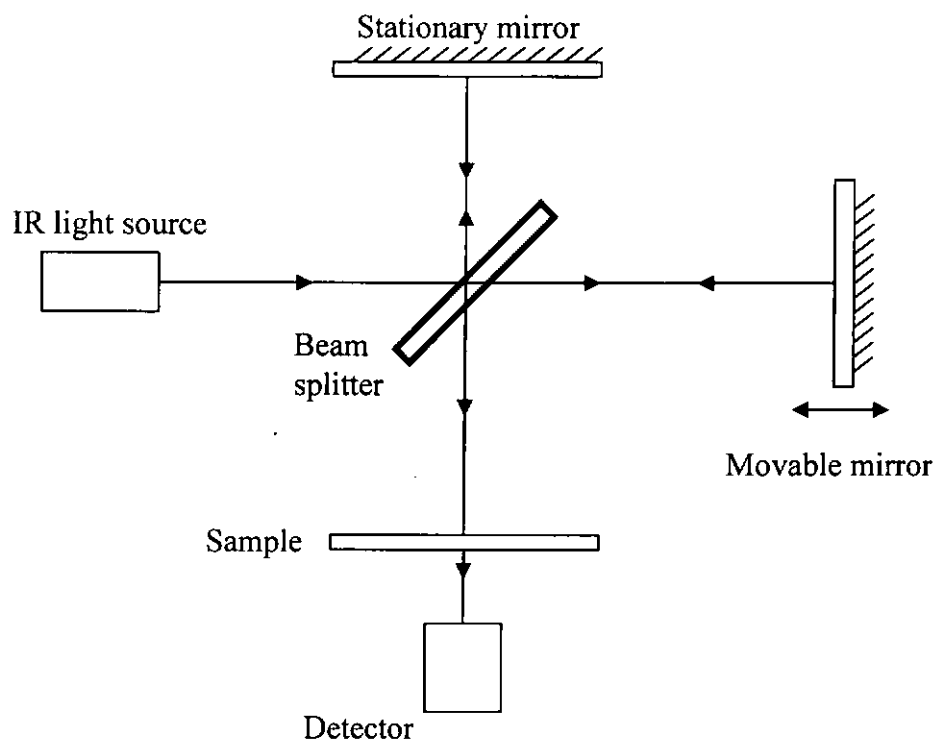


Fig. 2.7 The basic configuration of a FTIR spectrometer.



2.2.1.3 X-ray diffraction

X-ray diffraction (XRD) experiments were performed by using a Philip X'ERT system, with the use of CuK_α radiation at a wavelength of $\lambda = 0.154 \text{ nm}$. The system was used to investigate the crystallographic structure of the films. The standard 2θ - θ scanning spectra, 2θ scanning spectra with an incident glancing angle of 3° , and $(10\cdot1)$ pole figures and $(10\cdot1)$ ϕ -scan patterns of the films were recorded. As illustrated schematically in Fig. 2.8, when an x-ray beam shines on the sample, an x-ray beam is reflected from one lattice plane, and another x-ray is reflected by a lattice plane lying underneath (Fig. 2.9). The Bragg condition for constructive interference is (Fig. 2.8):

$$2d \sin\theta = \lambda$$

where d is the lattice spacing and 2θ is defined as the diffraction angle.

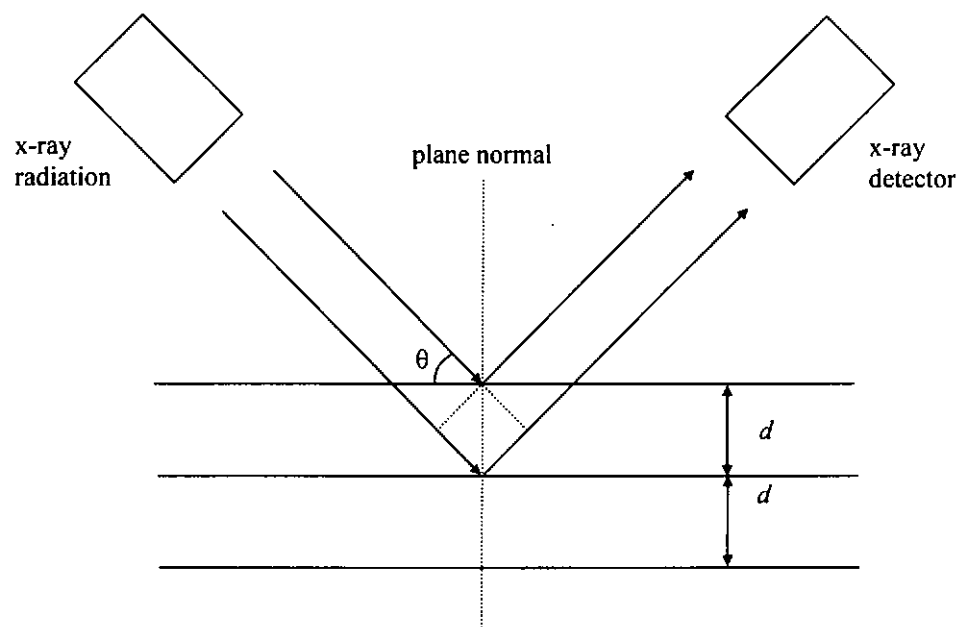


Fig. 2.8 Schematic diagram of the principle of X-ray diffraction.



The diffraction angle 2θ and d values of lattice planes of AlN are listed in Table 2.9.

2θ (deg.)	lattice plane	d (nm)
33.2	(10·0)	0.2695
36.1	(00·2)	0.2485
38.0	(10·1)	0.2365

Table 2.9 d space of three major AlN lattice planes. [Natl, 1975]

a.) 2θ - θ scan x-ray diffraction technique

For texture AlN films, the 2θ - θ spectrum shows a strong diffraction peak around 36.1° from the (00·2) planes, while the intensity of other peaks are relatively weak. Preferential c-axis orientation perpendicular to the substrate surface can thus be identified. For polycrystalline AlN films, due to the random orientation of the grains, all the above diffraction peaks should be detected.

b.) Glancing incident x-ray diffraction technique

Glancing incident x-ray diffraction (GIXD) is used to increase the interaction path between the x-ray beam and detected material. With this technique, the intensity of the diffraction peak is expected to be increased. In this experiment, the incident x-ray beam was aligned to shine on the sample with a glancing angle of 3° . The experimental configuration is shown in Fig. 2.10.

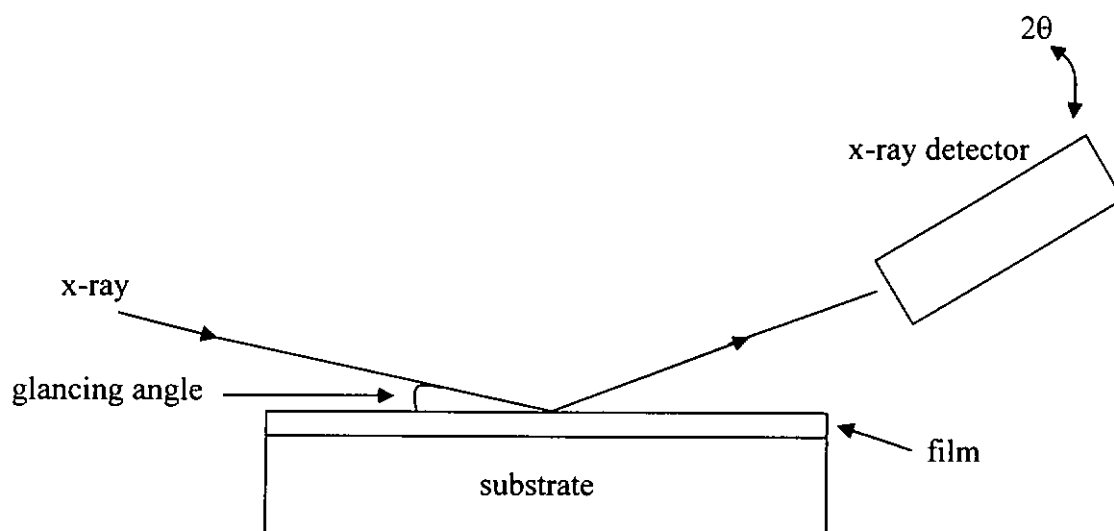


Fig. 2.10 Schematic diagram of glancing incident x-ray diffraction.

c.) Pole figure

Pole figure is a two dimensional projection of a hypothetical sphere surrounding the crystal which is used to analyze the in-plane preferential orientation of grains. Figure 2.11 shows the schematic diagram of pole figure experiment. During experiment, the 2θ angle is fixed whereas the ϕ angle and the ψ angle are varied from 0° to 360° and 0° to 90° , respectively. Any preferential orientation of the AlN (10·1) planes in the sample can be revealed with this experiment. According to the Bragg's Law, the 2θ angle should be set at 38° .

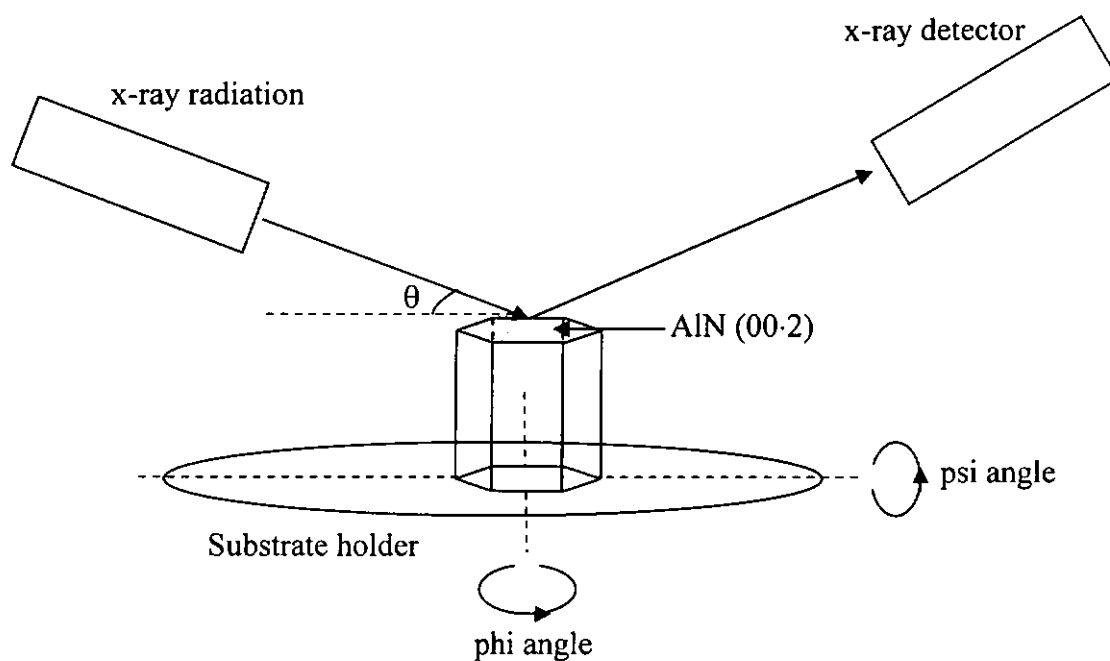


Fig. 2.11 Schematic diagram showing the set up for the observation of pole figure.



2.2.2. Piezoelectric coefficient measurements

AlN is a well-known piezoelectric material. When an electric field is applied to the material, a mechanical strain is induced, or vice versa. The relationship between the magnitude of the induced strain (x) and the applied voltage (V) is represented by the following equation:

$$x = d_{33} V \quad (\text{under zero stress condition}) \quad (2.1.1)$$

where d_{33} is the piezoelectric coefficient and x is the displacement along the same direction (Fig. 2.12).

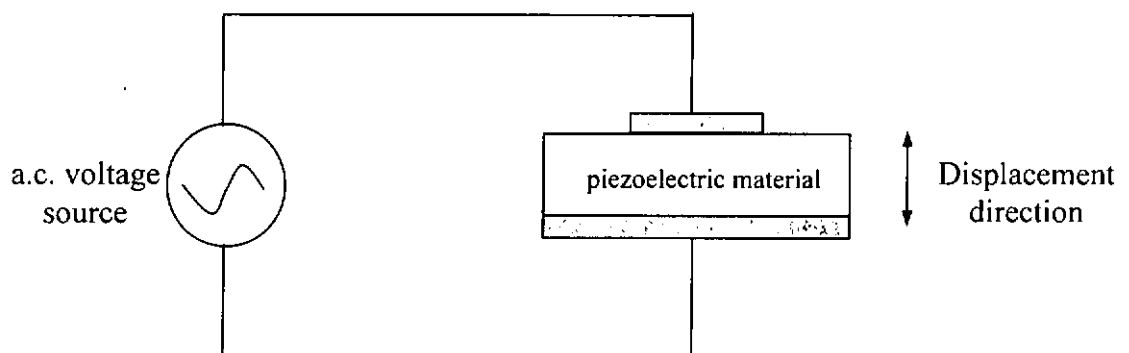


Fig. 2.12 Schematic diagram of a piezoelectric measurement.



There are many methods for measuring the d_{33} value. Atomic force microscopy (AFM) is a widely used method to determine the piezoelectric coefficient of the material. Rodriguez, *et al* [Rodriguez, 2002] used AFM to measure the d_{33} value of AlN films. In AFM, a voltage is applied to the piezoelectric material, and the vertical displacement of the probing tip in contact with the sample is measured simultaneously. The amplitude of the tip vibration is then enlarged by the lock-in amplifier. Finally the d_{33} value can be determined. Double beam interferometry technique is also frequently used [Burianova, 2001]. However, the alignment and its operation are relatively complicated. Zhang *et al* [Zhang, 1988] used a single beam Michelson interferometer to detect surface displacement of the sample. In this study, a similar experiment setup is applied to measure the d_{33} value of the AlN films.

In this study, a single beam laser interferometry technique is used to measure d_{33} value of the AlN films deposited on Pt(111)/Si(100) substrates. Displacement due to piezoelectric effect is in the order of the pico-meter, and so the measurement is required to have very high accuracy. In addition, the precision of the measurement is also affected by the clamping effect due to the substrate. As shown in Fig. 2.13, the film adheres to the substrate firmly, so that when a voltage is applied to the piezoelectric film, it expands or contracts such that a stress field is generated in the interior of the substrate. Fig. 2.13 shows the bending of the system. At such, the deformation of the film on the top of the substrate is affected to some extent. This causes the piezoelectric response to be different from (usually smaller than) that in the case of a free-standing film.

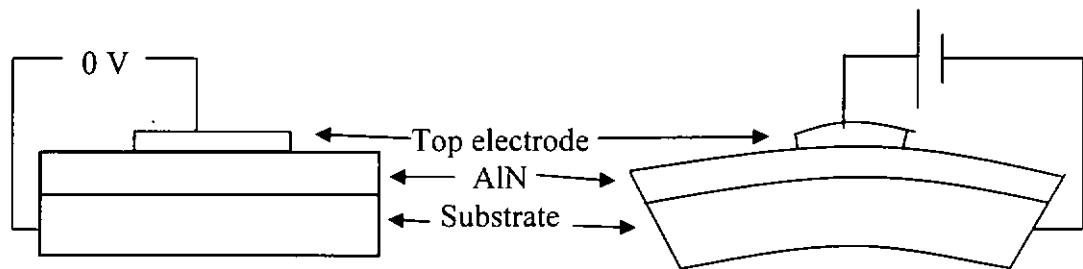


Fig. 2.13 Schematic diagrams showing the clamping effect of a film for the measurement of d_{33} .



In the single beam laser interferometer measurement, a He-Ne laser beam (L) of wavelength $\lambda_L = 632.8$ nm is linearly polarized. The beam has a frequency of f_L . The beam L is split into two, i.e. the reference beam R and probe beam P, by a beam splitter. The beam R passes through the Dove prism, whereas the beam P is through the Bragg cell which is inserted between the two beam splitter. The frequency of beam P is shifted by f_B (70 MHz) when passing through the Bragg cell. The frequency of the P beam becomes $f_L + f_B$, and is directed to shine on the top electrode of the AlN sample. At the same time, an ac electric field is applied across the top and bottom electrodes of the AlN film sample by using a function generator (Sony Telclonix AFG310). The frequency of the excitation voltage is 15 kHz. A digital storage oscilloscope (HP 54645A, Hewlett-Packard) was used to measure the voltage applied by the function generator. After being reflected by the top electrode of the sample, the phase of the beam P is modulated by the oscillation of the sample surface. The reflected beam is denoted by the beam S thereafter. The beam R and S join together at the beam splitter, and the resultant intensity is finally detected by a photodetector. The phase difference of the beams R and S is then detected and converted to give the amplitude of the oscillation of the AlN film surface. The data are recorded by a lock-in amplifier and a spectrum analyzer simultaneously in order to compare with each other. The d_{33} value of the sample can then be calculated by equation 2.1.1.

In this study, the values of d_{33} of AlN films were measured by using a Mach-Zehnder type heterodyne (single beam) laser interferometer (SH-120, B.M. Industries, France). The schematic diagram of laser interferometer is shown in Fig. 2.14.

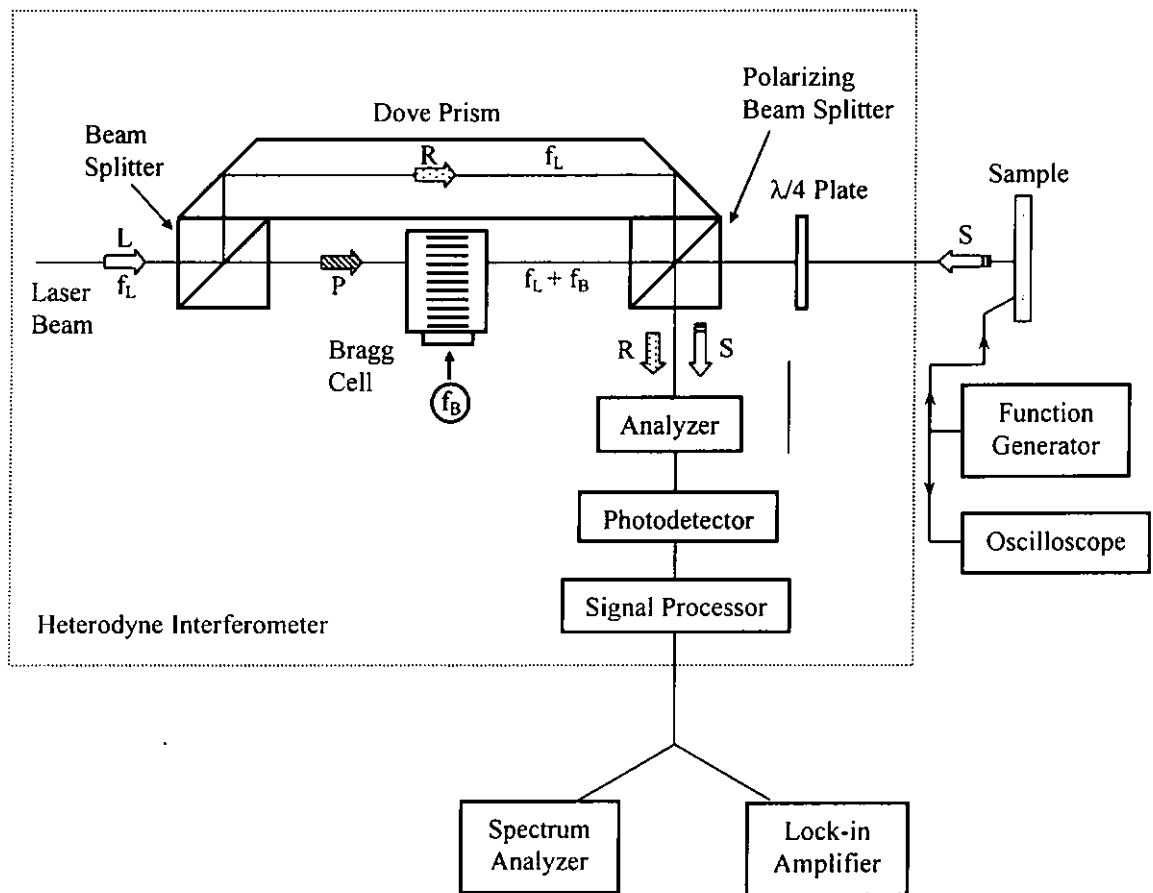


Fig 2.14 Schematic diagram of the single beam laser interferometer for the measurements of piezoelectric coefficient.



The top electrodes are so small (radius = 0.45×10^{-3} m) that the conducting wires must be bonded to the electrodes by using an ultrasonic wire bonder. The sample is fixed to a PCB board by wax for the convenience of measurements.

2.2.3. Impedance analysis

A HP 4194A Hewlett Packard impedance/gain phase analyzer was used to investigate the capacitance (C_s) and dielectric loss (δ) of the AlN films in a frequency range of 100 Hz – 1 MHz. The AlN films deposited on Pt(111)/Si(100) substrates were used for the measurements. Al top electrodes were made on the surface of the AlN films. The samples are in a parallel plate configuration. From the measured value of C_s , the dielectric constant (ϵ) can be calculated by:

$$C_s = \frac{\epsilon \epsilon_0 A}{d}$$

where $\epsilon_0 = 8.85 \times 10^{-12}$ and ϵ is the dielectric constant of the material. A is the area of the top electrode and d is the thickness of the film. Normally, an AlN film can be treated as an equivalent circuit as shown in Fig. 2.15:

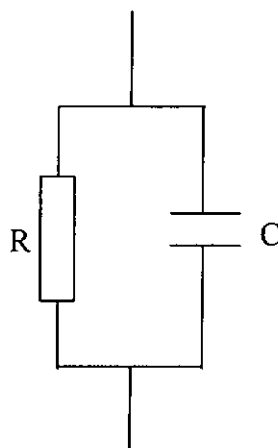


Fig. 2.15 The equivalent circuit of an AlN film.



2.2.4. Mechanical properties

Hardness (H) and Young's Modulus (E) of the AlN films are investigated in this study. A nanoindenter (Nano Instruments Inc., Model IIs) having a Berkovic 3-sided diamond indenter tip was used to evaluate the value of H and E of the AlN film samples. The half-included angle of the tip is 65.3° . The upper end of the indenter shaft has a permanent magnet, which is coupled to a coil. The lower end has a diamond indenter tip. Load is applied by passing a current through the coil. The displacement of the tip is measured by a capacitance displacement gauge. During an indentation experiment, both the signals of load and displacement are recorded by a computer. In particular, a nanoindenter is designed to operate in a low load range of $1 \mu\text{N} \sim 500 \text{ mN}$. The resolution of depth is around a few nanometers. Therefore, the machine is particular useful to probe the mechanical properties of a film sample on substrate. Measurements are performed at shallow depths ($1 - 2000 \text{ nm}$) and extremely low loads ($20 \mu\text{N} - 400 \text{ mN}$), so that the results are assumed not affected by the deformation of the substrate material.

The hardness (H) of a sample is defined by the following relationship:

$$H = \frac{P_{\max}}{A(h_c)}$$

As shown in Fig. 2.16, P_{\max} is the load applied to the sample by the tip, $A(h_c)$ is the cross-section area (projected area) of the tip associated with the contact depth h_c . h_c is the contact depth associated with the periphery of the contact surface between the tip and the film.

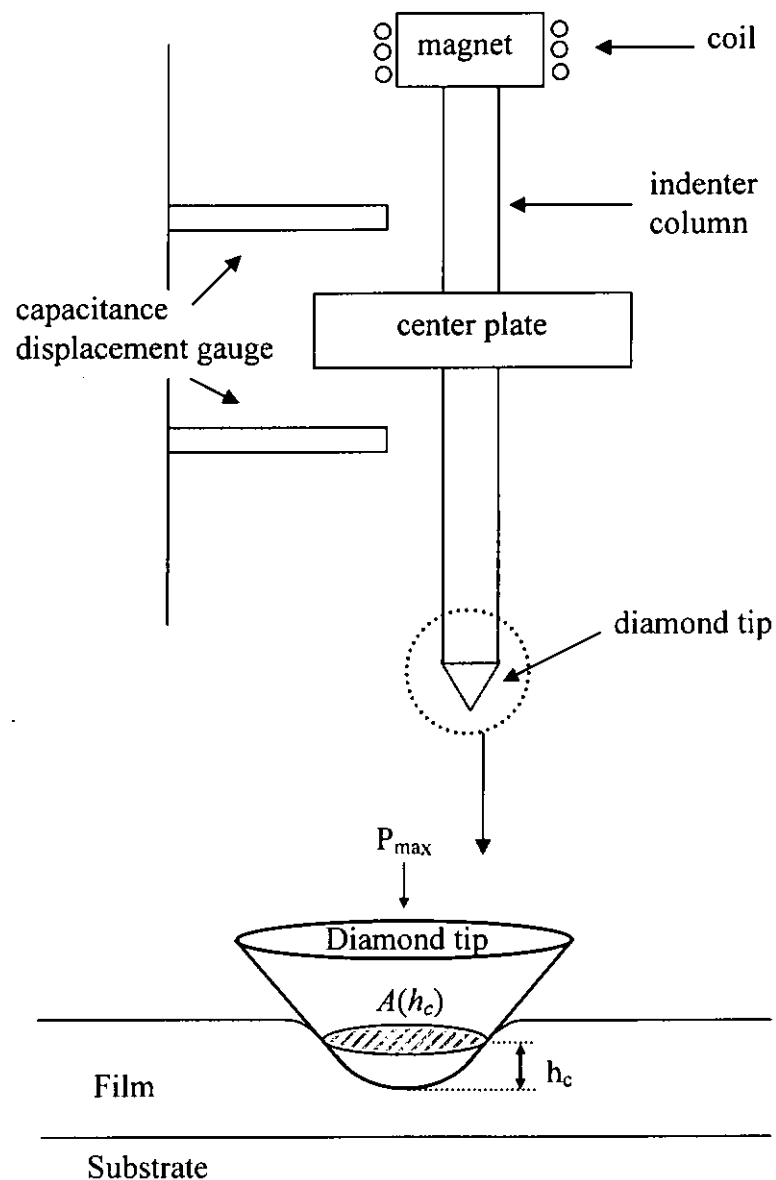


Fig. 2.16 A schematic presentation nanoindenter test.



Load and displacement data are recorded simultaneously to produce the load-unload curve as shown in Fig. 2.17. The young's modulus of an indented sample can be obtained from the equation:

$$S = \frac{2}{\sqrt{\pi}} E_r \sqrt{A(h_c)}$$

where S is equal to the slope of the unloading curve at the maximum load.

The E_r is the reduced elastic modulus of the sample defined as:

$$E_r = \left[\frac{1 - \nu_i^2}{E_i} + \frac{1 - \nu_s^2}{E} \right]$$

where E is the young's modulus of the sample. ν_i and E_i are 0.07 and 1141 GPa are the Poisson's ratio and elastic modulus of the diamond tip, respectively. The Poisson's ratio of the film samples is assumed to be 0.25.

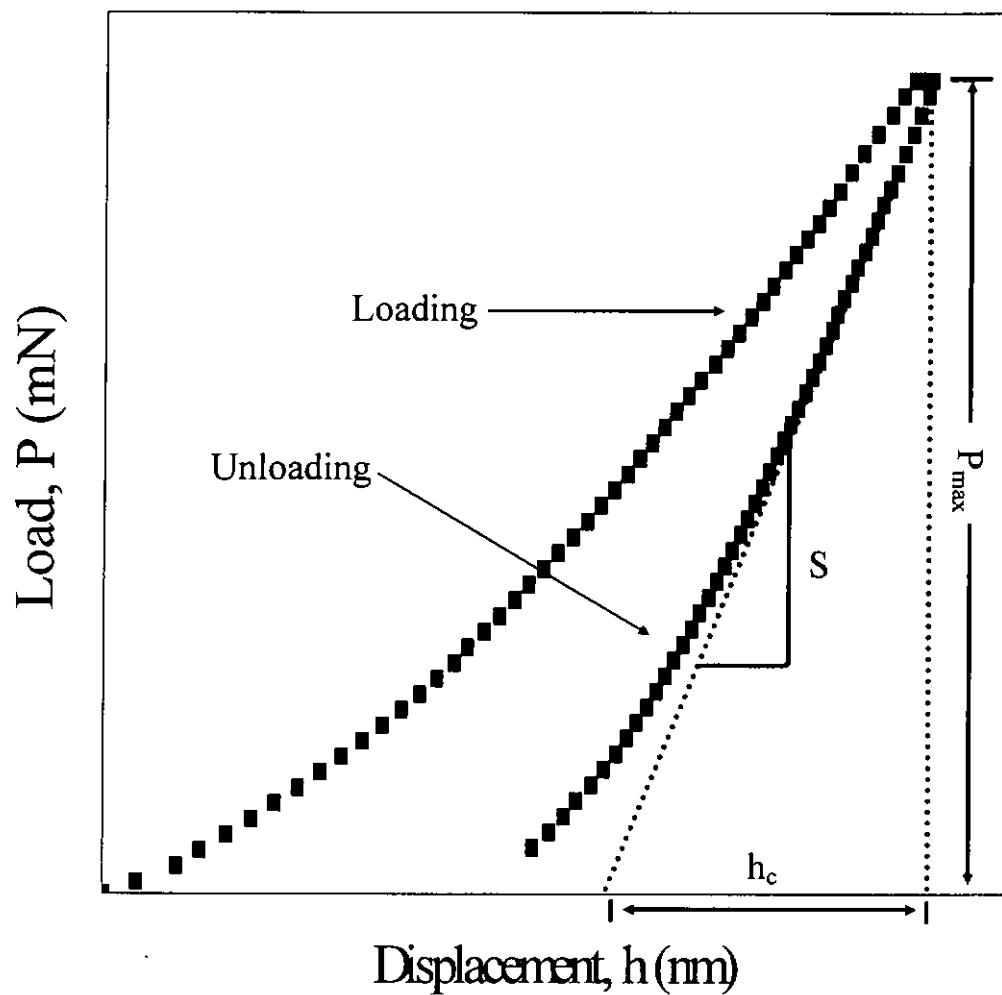


Fig. 2.17 Typical load-unload curves obtained in a nanoindentation experiment.



Six different indentation experiments were designed as shown in Table 2.18. Each experiment consists of an approach segment, three load-hold-unload cycles with successively increased normal loads, a thermal drift correction segment and a completely unload segment. The loads for the six indentation experiments are set as shown in Table 2.18.

Experiment	Indentation	Maximum load (mN)		
1	1-15	0.02	0.1	0.3
2	16-30	1	2	3.4
3	31-45	3	7.5	15
4	46-50	30	60	90
5	51-55	100	200	300
6	56-60	95	250	400

Table 2.18 The settings of maximum loads for the six nanoindentation experiments.

Experiments 1-3 were repeated fifteen times at different positions on a film surface in order to get an average result. Experiments 4 – 6 were repeated five times. Totally 60 indentations arranged in a 10 x 6 array were made on each sample. Any two adjacent indents were arranged to separate by a distance of 50 μm . The data points show some scattering due to the noise caused by the vibration of the system and surrounding environment. The surface roughness of the sample also causes some fluctuation of the data.



Chapter 3

Preparation Condition Dependence of AlN Film Structure

In this Chapter, the preparation condition dependence of the structure of the RMS AlN films is presented and discussed.

3.1 Summary of AlN sample fabrication parameters

Several series of AlN thin films were fabricated at different sputtering conditions as listed in Table 3.1. The substrate temperature (T_s), RF power (P_w), sputtering pressure and Ar/N₂ gas ratio were varied as the deposition parameters. The corresponding changes in the film structure were investigated. The processes were designed such that only one parameter was changed, such the corresponding change of the film structure due to that parameter can be investigated.

As listed in Table 3.1, samples of series I were prepared with the sputtering pressure varying from 5 to 10 mTorr. T_s , P_w and gas ratio Ar/N₂ were fixed at 450°C, 180 W and 5 : 7 respectively. The two samples of series II were prepared at gas ratios of 8 : 2 and 2 : 8, while T_s , P_w and sputtering pressure were fixed at room temperature (RT), 100 W and 5 mTorr. Samples of series III were prepared at P_w varying from 100 to 250 W, where T_s , sputtering pressure and gas ratio were fixed at 700°C, 5 mTorr and 2 : 8. Films of series IV were prepared at T_s varying from RT to 700°C,



where P_w , sputtering pressure and gas ratio were fixed at 250 W, 5 mTorr and 2 : 8. In all experiments, the target-to-substrate distance (D) is set to be 10 cm.

Series	Sample code (AlN#)	T_s ($^{\circ}\text{C}$)	P_w (W)	Sputtering pressure (mTorr)	Deposition time (min)	Gas ratio (Ar : N ₂)	Thickness (nm)	Coating rate (nm min ⁻¹)
I	40	450	180	5	90	5 : 7	700	7.78
	31	450	180	7	90	5 : 7	585	6.51
	29	450	180	8	150	5 : 7	995	6.63
	39	450	180	10	90	5 : 7	400	4.44
II	45	*RT	100	5	90	8 : 2	500	5.56
	46	*RT	100	5	90	2 : 8	250	2.78
III	47	700	100	5	90	2 : 8	210	2.33
	48	700	210	5	90	2 : 8	400	4.44
	49	700	250	5	90	2 : 8	500	5.56
IV	52	*RT	250	5	90	2 : 8	560	6.23
	50	100	250	5	90	2 : 8	510	5.69
	53	300	250	5	90	2 : 8	480	5.31
	51	500	250	5	90	2 : 8	515	5.73
	49	700	250	5	90	2 : 8	500	5.56

*RT = Room Temperature

Table 3.1 Deposition conditions, thickness and coating rate of AlN films.



3.2 Thickness and coating rate

The thicknesses of the AlN films deposited on Si(100) substrates were measured, and were found to vary from 210 to 700 nm (Table 3.1). The coating rates were calculated and found to fall in the range of 2.78 – 7.78 nm min⁻¹. The coating rate was rather sensitive to the change in the deposition conditions.

First, the coating rate of the films of series I dropped monotonically from 7.78 to 4.44 nm min⁻¹ when the sputtering pressure increased from 5 to 10 mTorr. This trend was plotted in Fig. 3.2 (a). This result is explained by considering that when the ambient pressure increases, the mean free path (λ) of the species in the chamber decreases. As a consequence, the species sputtered from the target, and those generated in the plasma zone would be scattered more severely before reaching the substrate surface. This increases the random thermal motion of the particles, and hence the coating rate drops.

Second, Table 3.1 reveals that the rise in Ar/N₂ ratio results in an increase of the coating rate. This is because more Ar⁺ ions are generated in the plasma zone, giving rise to a higher sputtering rate of Al. This enriches the Al content in the deposits.



Fig. 3.2 (b) and (c) show the variation of the coating rate as a function of substrate temperature (T_s) and RF power (P_w), respectively. Results show that the coating rate is insensitive to T_s varying in a wide range from room temperature to 700°C. The result indicates that the sticking coefficient of the species generated in the process is not affected by the temperature of the substrate surface.

Fig. 3.2 (c) shows that the coating rate increases with increasing P_w . This result is expected since higher input power increases the plasma density, and generates more particles to bombard the target. The coating rate is increased as a result.

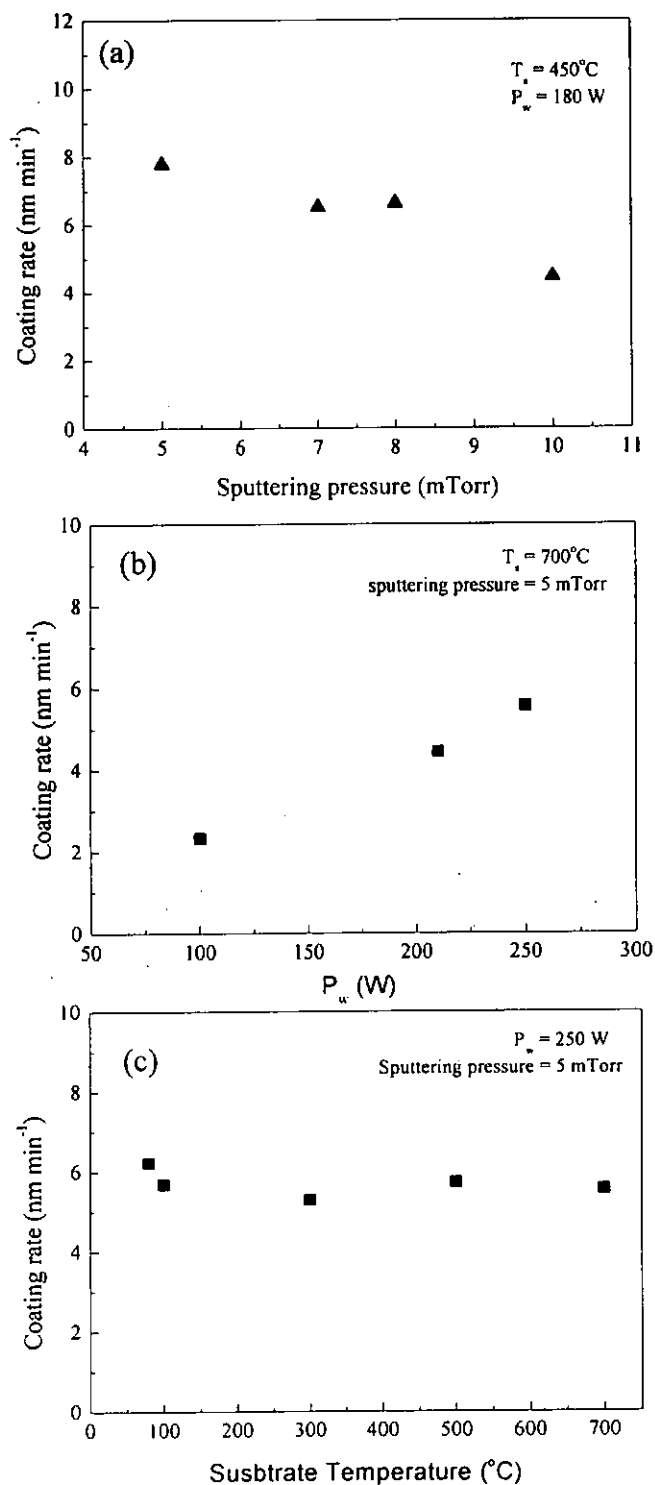


Fig. 3.2 Coating rate of AlN films as a function of (a) sputtering pressure, (b) P_w and (c) T_s .



Compared with some published data, we note that Ivanov *et al* [Ivanov, 1995] reported a coating rate of 16.7 nm min^{-1} for RMS AlN films, which was much higher than the maximum rate of 7.8 nm min^{-1} that we recorded in this study. This difference was explained considering that Ivanov *et al* used a lower sputtering pressure of 2 mTorr, and a higher P_w of 300 W. According to our present results, a lower sputtering pressure and/or higher P_w can give a higher coating rate of AlN films.

In addition, Kim *et al* [Kim, 1998] used a higher sputtering pressure of 6.3 mTorr and a target power of 40 W to result in a coating rate of about $16\text{--}17 \text{ nm min}^{-1}$ for RMS AlN films. This coating rate was much higher than that we achieved in this study. The reason is that the target-to-substrate distance (D) used by Kim *et al* was 3 cm, which was much smaller than 10 cm used in our sputtering processes. The use of a shorter D allows more sputtered species to reach the substrate without being scattering, so that the coating rate is increased as a result.



3.3 Four types of AlN film structures

In this section, we define four types of film structures that are found to form by our RMS processes. These four types of structures are named as (i) nearly amorphous AlN (na-AlN), polycrystalline AlN (p-AlN), texture AlN (t-AlN) and epitaxial AlN (e-AlN) structures. We then describe how the film structure is correlated with the settings of the fabrication conditions. Possible mechanisms leading to the formation of those structures will be discussed.

3.3.1 Nearly amorphous AlN structure

A film is defined to nearly amorphous (na-) AlN if its XRD data show the features as shown in Fig. 3.3. The spectra shown in Fig. 3.3 are the XRD 2θ - θ scan spectra and GIXD scan spectra of AlN films deposited on three different substrates, Si(100), Pt(111)/Si(100) and $\text{Al}_2\text{O}_3(00\cdot1)$ substrates, at $T_s = 100^\circ\text{C}$ and $P_w = 250\text{ W}$. The 2θ - θ spectra do not contain any visible diffraction peak. This indicates that the level of crystallization of these films is very low. Even if some crystallites may exist, their size must be very small, and would not have any preferred orientation. However, the GIXD scan spectra (recorded at a glancing angle of 3°) show some weak diffraction peaks associated with the (10·0), (00·2) and (10·1) AlN planes at $2\theta = 33.2$, 36.2 and 38.0 , respectively. The appearance of these peaks confirms that some crystallites are indeed present in the films. Since the peaks are so weak and broad, the crystallite size is further confirmed to be small and randomly oriented. Furthermore,



the relative intensities of the peaks are roughly consistent with those of the standard diffraction spectrum of AlN powder [Natl., 1975]. This further confirms that the orientation of the crystallites is really extremely random. The crystallites are assumed to be embedded in a random matrix, whereas the matrix is expected to retain the short range order of the AlN crystal structure. This conjecture is supported by the IR absorption data as described in the following context. A film of above features is classified to be a na-AlN film in this study. The na-AlN structure is different from the concept of “amorphous” (or “x-ray amorphous”), since the latter is defined to be a completely random atomic network containing no any crystallites.

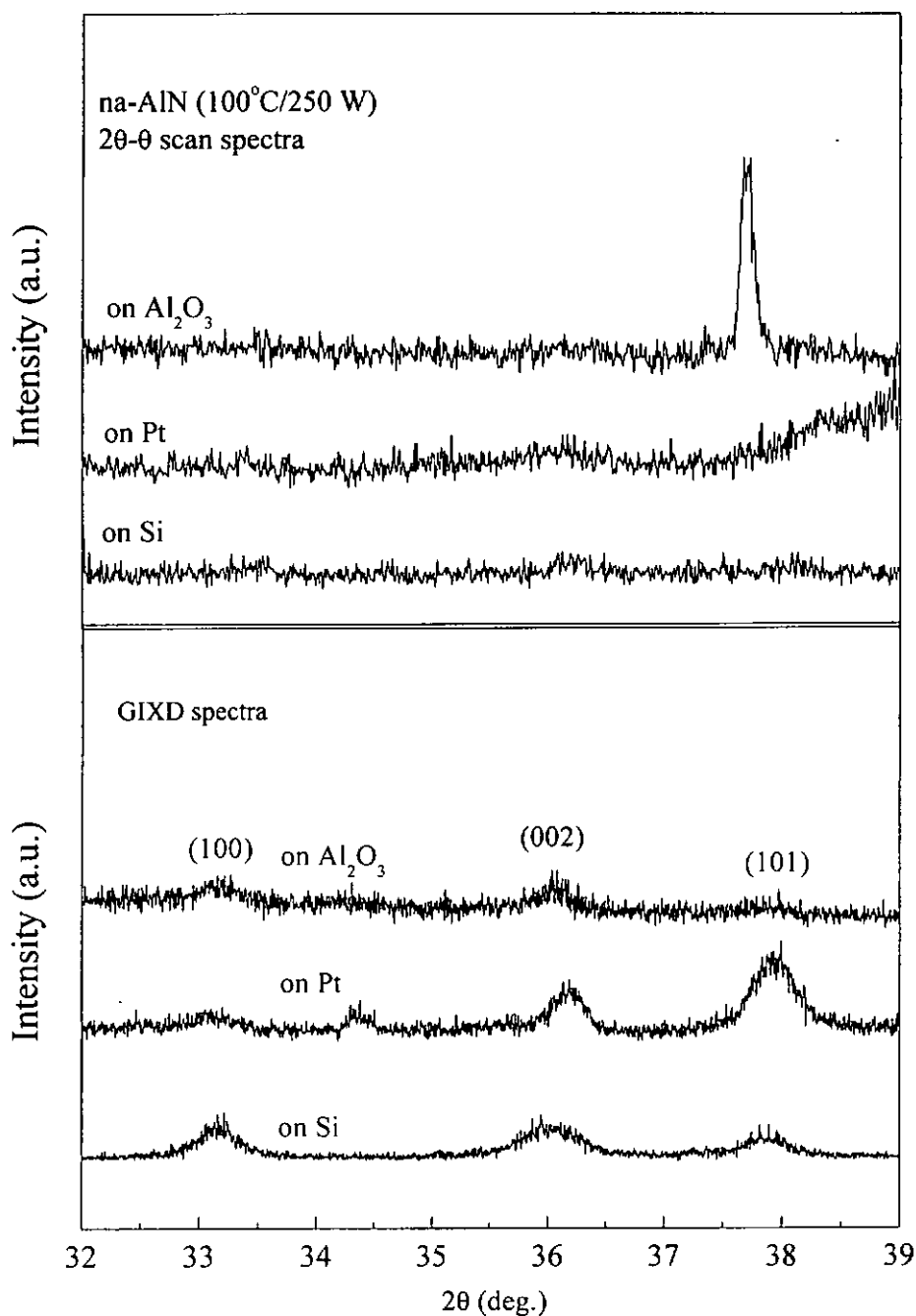


Fig. 3.3 Typical XRD 2θ - θ spectra and GIXD spectra (glancing angle = 3°) of na-AlN films deposited on the three different substrate materials, at $T_s = 100^\circ\text{C}$ and $P_w = 250\text{ W}$.



3.3.2 Polycrystalline AlN structure

A film is defined to be a p-AlN film if its XRD spectrum shows the features of the spectra shown in Fig. 3.4. The XRD 2θ - θ scan spectra shown in Fig. 3.4 are the 2θ - θ scan spectra of the three p-AlN films deposited on Si(100), Pt coated Si and sapphire, respectively. Some diffraction peaks can be seen. Their 2θ fell in the range from 32 to 39° , and was consistent with the diffraction angles of the (10-0), (00-2), and (10-1) planes of the crystalline AlN structure. No other diffraction peak can be observed outside this range. The above results indicate that some AlN grains exist in the film. Their average size can be estimated by the equation $B = \frac{0.9\lambda}{t \cos \theta}$ [Cullity, 2001], where B is the full width of half maximum (FWHM) of the diffraction peak in radian, t is the diameter of the grain and λ is the wavelength of the x-ray. The average size of the grains in a p-AlN film should therefore be larger than those in a na-AlN film. In addition, the relative intensities of the peaks do not change with the variation of the incident angle of the x-ray beam. This confirms that the AlN grains in p-AlN film should not have strong preferential orientation.

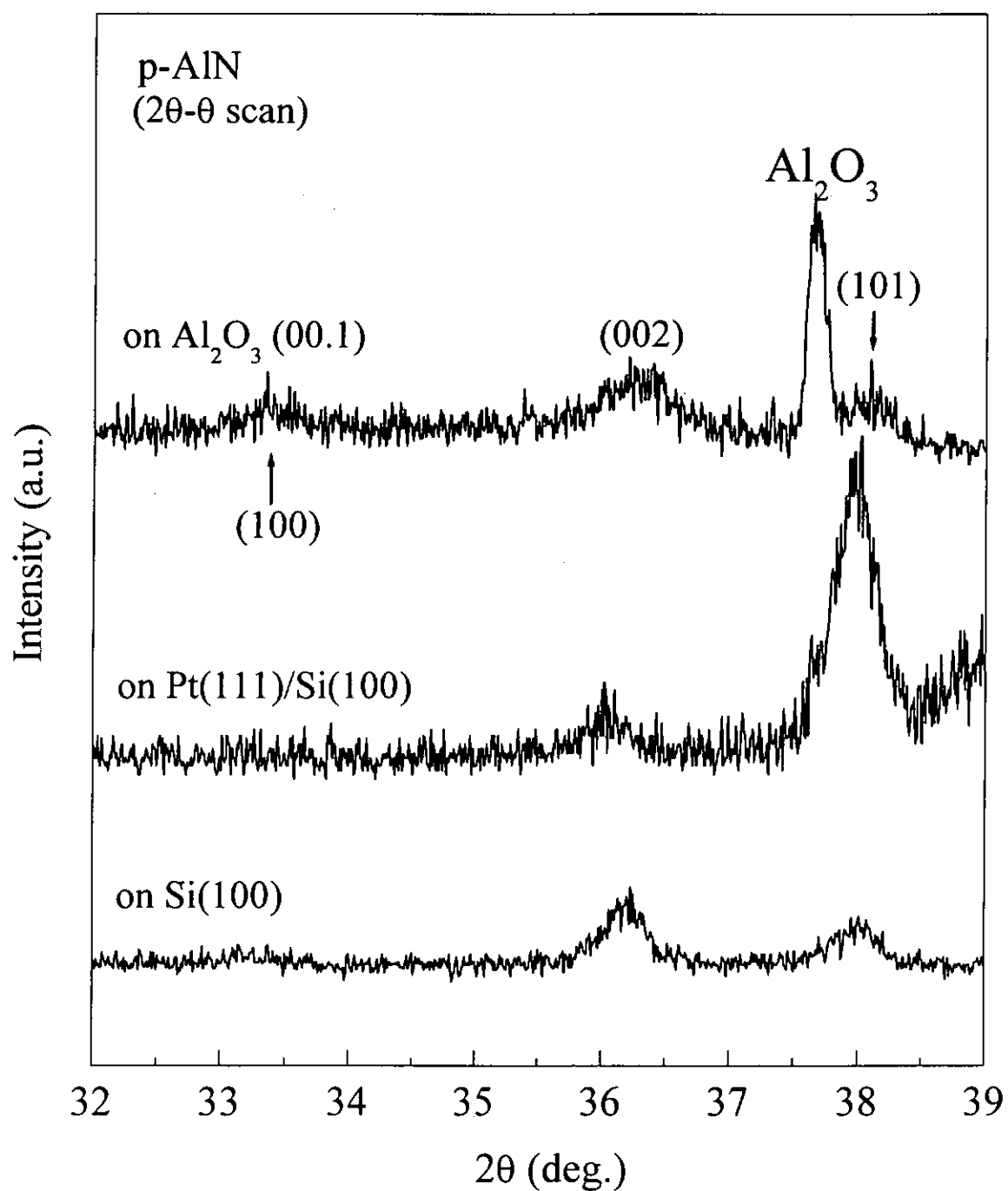


Fig. 3.4 Typical 2θ-θ scan spectra of p-AlN films deposited on three different substrate materials.

3.3.3 Texture and epitaxial AlN structures

The 2θ - θ spectra of a t-AlN film and an e-AlN film are very similar, as shown in Fig. 3.5 and Fig. 3.6. Both of them exhibit a single peak associated with the (00-1) AlN planes, indicating that in these films the AlN grains are strongly oriented with their c-axis perpendicular to the film surface. However, for a film of (00-1) texture, the a- and b-axis of the grains have random orientation on the plane of the substrate. Differently, for a film of the epitaxial structure, the a- and b- axes are well aligned. The schematic illustrations of these two different types of structures are shown in Fig. 3.7.

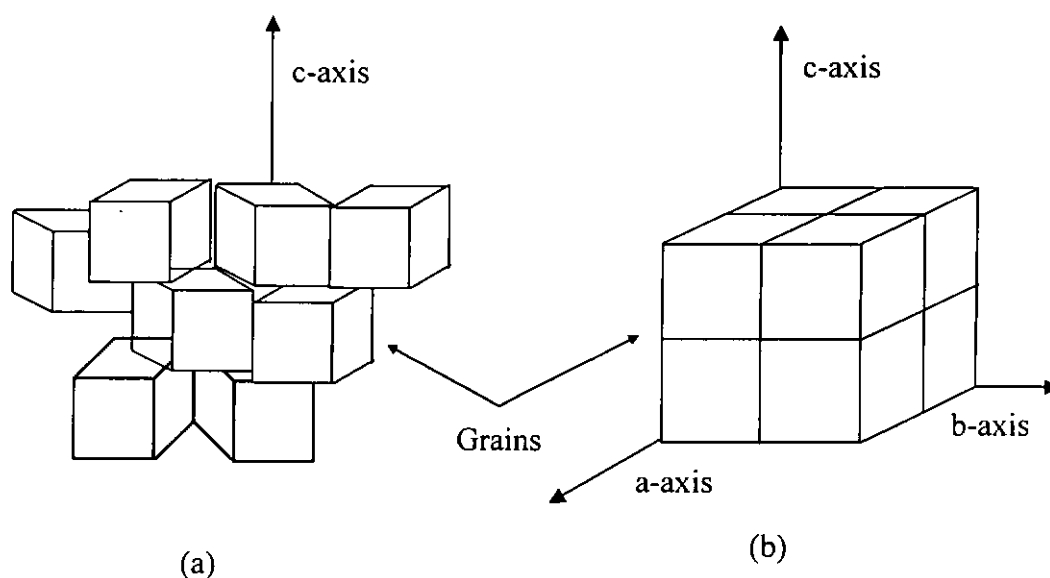


Fig. 3.7 The schematic diagrams of the (a) t-AlN and (b) e-AlN structures.

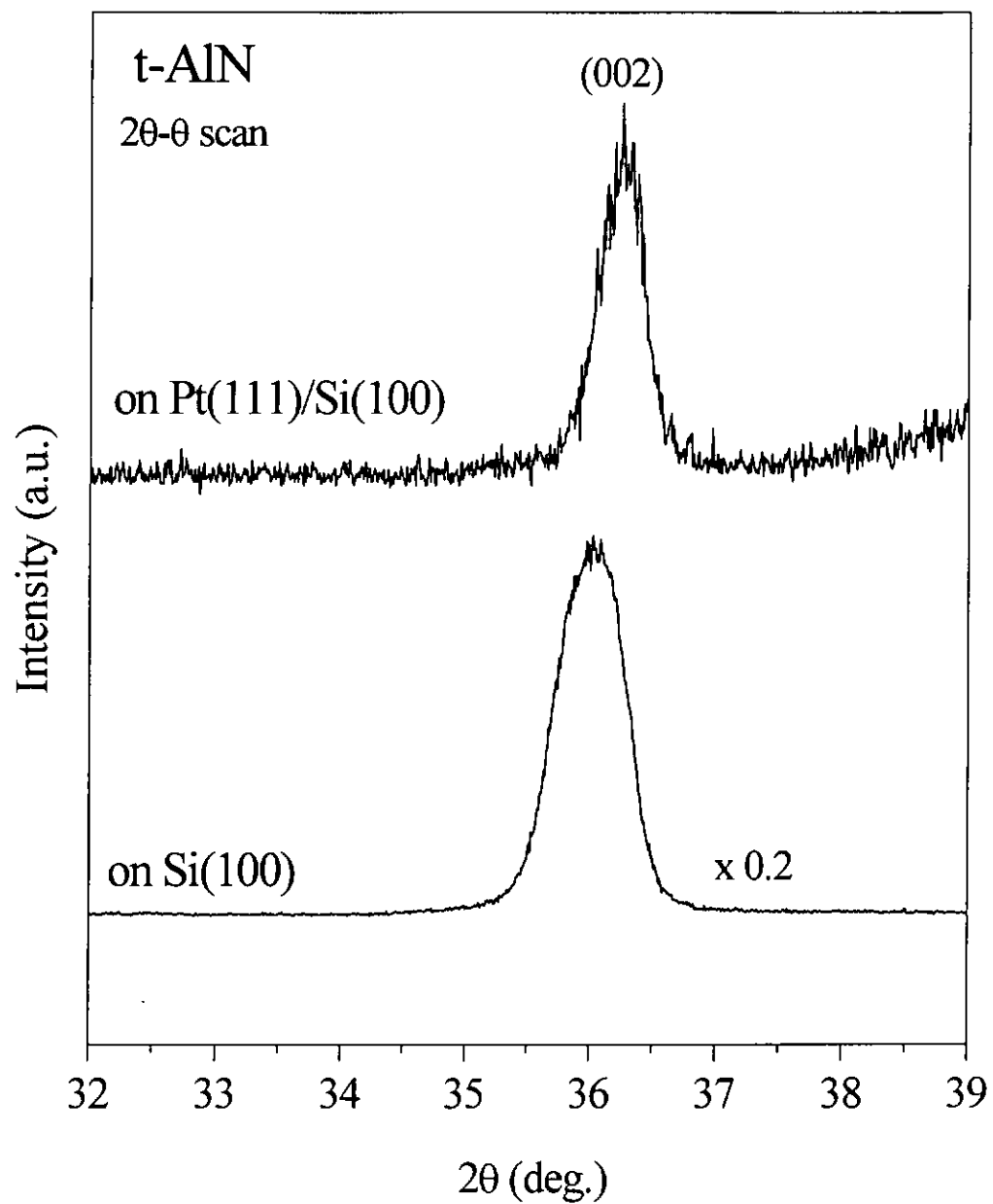


Fig.3.5 Typical 2θ - θ scan of t-AlN films deposited on Si(100) and Pt(111)/Si(100) substrates.

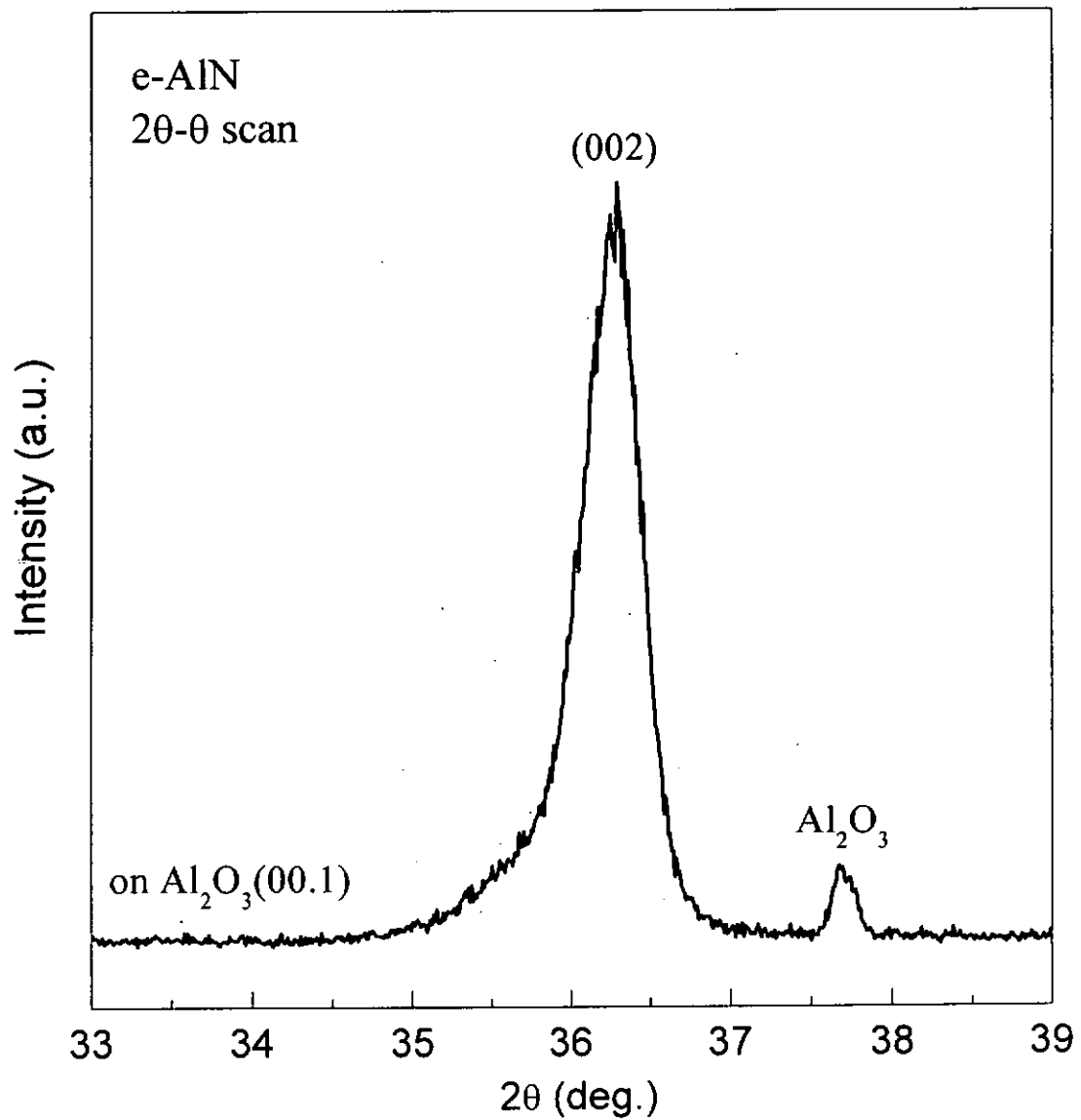


Fig. 3.6 Typical 2θ - θ spectra of e-AlN films deposited on $\text{Al}_2\text{O}_3(00.1)$ substrate.



In a t-AlN film and an e-AlN film have the c-axes of the grains are aligned along the normal of the substrate. Therefore, their 2θ - θ XRD spectra are presumably to be identical. To reveal the structural difference between the two, one may refer to their pole figure, and ϕ -scan, which provide additional information on the alignment of the a- and b- axes on the surface of the substrate.

To record the (10·1) pole figure of a t-AlN film, 2θ was set at 38° according to the Bragg's Law. As shown in Fig. 3.9 (a), the poles of the AlN (10·1) planes are found to locate uniformly in a circle with a psi angle $\approx 61.5^\circ$. It is equal to the angle between a AlN (10·1) plane and a AlN (00·2) plane. The distribution of the poles of the AlN (10·1) planes as observed confirms that the grains rotate randomly about their c-axis, and so the film structure is classified to have texture.

Fig. 3.9 (b) shows the (10·1) pole figure of another sample. The poles of the (10·1) AlN planes appear in the form of spots in the figure, showing orderly alignment of the a- and b-axis on the substrate surface. In the figure, six (10·1) poles were found, showing a six-fold symmetry consistent with the symmetry of the locations of the (10·1) AlN plane in the AlN crystal structure. All these features confirm the epitaxial structure of an e-AlN film. Moreover, six diffraction peaks of the (10·1) AlN planes are recorded in the ϕ -scan pattern as shown in Fig. 3.10 (a). Two adjacent peaks are separated by a ϕ angle of 60° , showing again a six-fold symmetry.

In addition, the positions of these six peaks coincide with the six peaks of the (11·3) Al_2O_3 substrate. It shows that the (00·2) plane of the AlN film matches with the (00·1) Al_2O_3 substrate, with the [010] AlN direction to make an angle of 30° with the [010] Al_2O_3 direction shown in Fig 3.8.

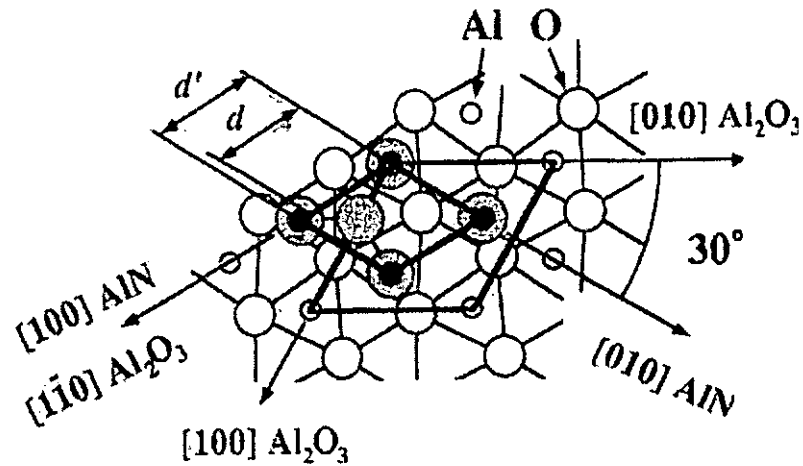


Fig 3.8 Top view of the epitaxial relation between AlN (00·1) and Al_2O_3 (00·1) [Sun, 1994].

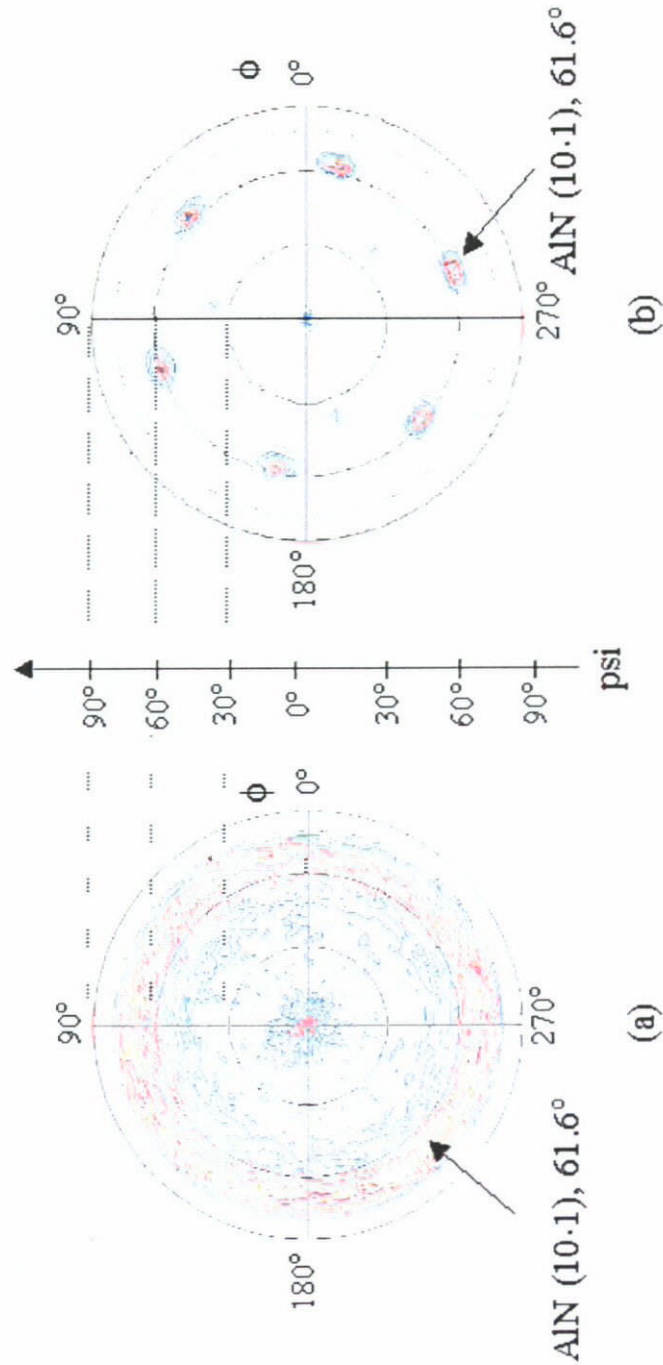


Fig. 3.9 Pole figure of (a) t-AlN film deposited on Pt(111)/Si(100) and (b) an e-AlN film deposited on $\text{Al}_2\text{O}_3(00.1)$ substrates.

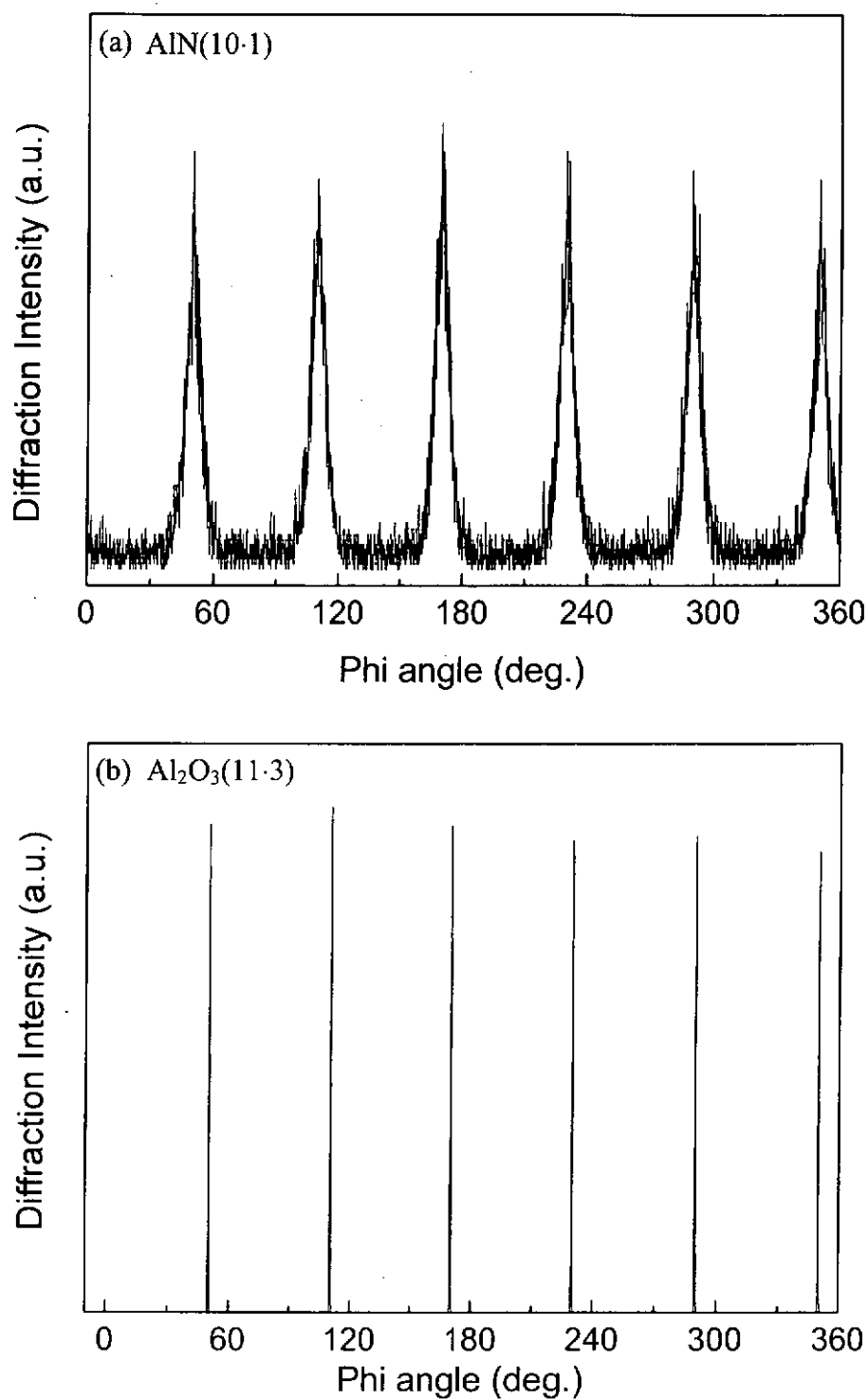


Fig. 3.10 ϕ -scan of an e-AlN film deposited on Al₂O₃(00-1) substrates.



3.4. T_s and P_w dependence of AlN film structure

The crystallographic structure of AlN films is affected by many factors, including the substrate temperature (T_s), RF power fed into the sputtering device (P_w), ambient pressure, target-to-substrate distance (D), and composition of the reactant gases. In addition, Lim *et al* [Lim, 2001] revealed that the selection of the substrate material affected significantly the preferred orientation of the grains. Different authors selected different sets of the parameters to study, and the parameters were varied. Consequently, it is difficult for the authors to have a consensus on the correlation between the deposition conditions and the film structure. In our study, we found that T_s and P_w , and the selection of substrate materials are the most critical factors for determining the film structure. Therefore, in this chapter, we concentrate to report the results caused by these three factors. Results are compared with those reported by many other groups. Some common trends between the data of different groups are found, and the physical reasons underlying these trends are discussed.



3.4.1 T_s - P_w diagram

In this section, we define T_s - P_w diagram to present the influences of T_s and P_w on the film structure. In a T_s - P_w diagram, T_s covers the range from room temperature to 700°C, and P_w from 100 to 250 W.

Fig. 3.11 (a), (b) and (c) are the three T_s - P_w diagrams for the films deposited on Si(100), Pt(111)/Si(100) and $\text{Al}_2\text{O}_3(00\cdot1)$, respectively. Each T_s - P_w diagram is divided into many regions. Each of Fig. 3.11 (a) and (b) is divided into a na-AlN region, a p-AlN region and a t-AlN region. Each region corresponds to the ranges of T_s and P_w at which a specific film structure is formed. Fig. 3.11 (c) is also divided in three regions. Other than the na-AlN, p-AlN regions, an e-AlN region is identified, instead of a t-AlN region as seen in Fig 3.11 (a) and (b).

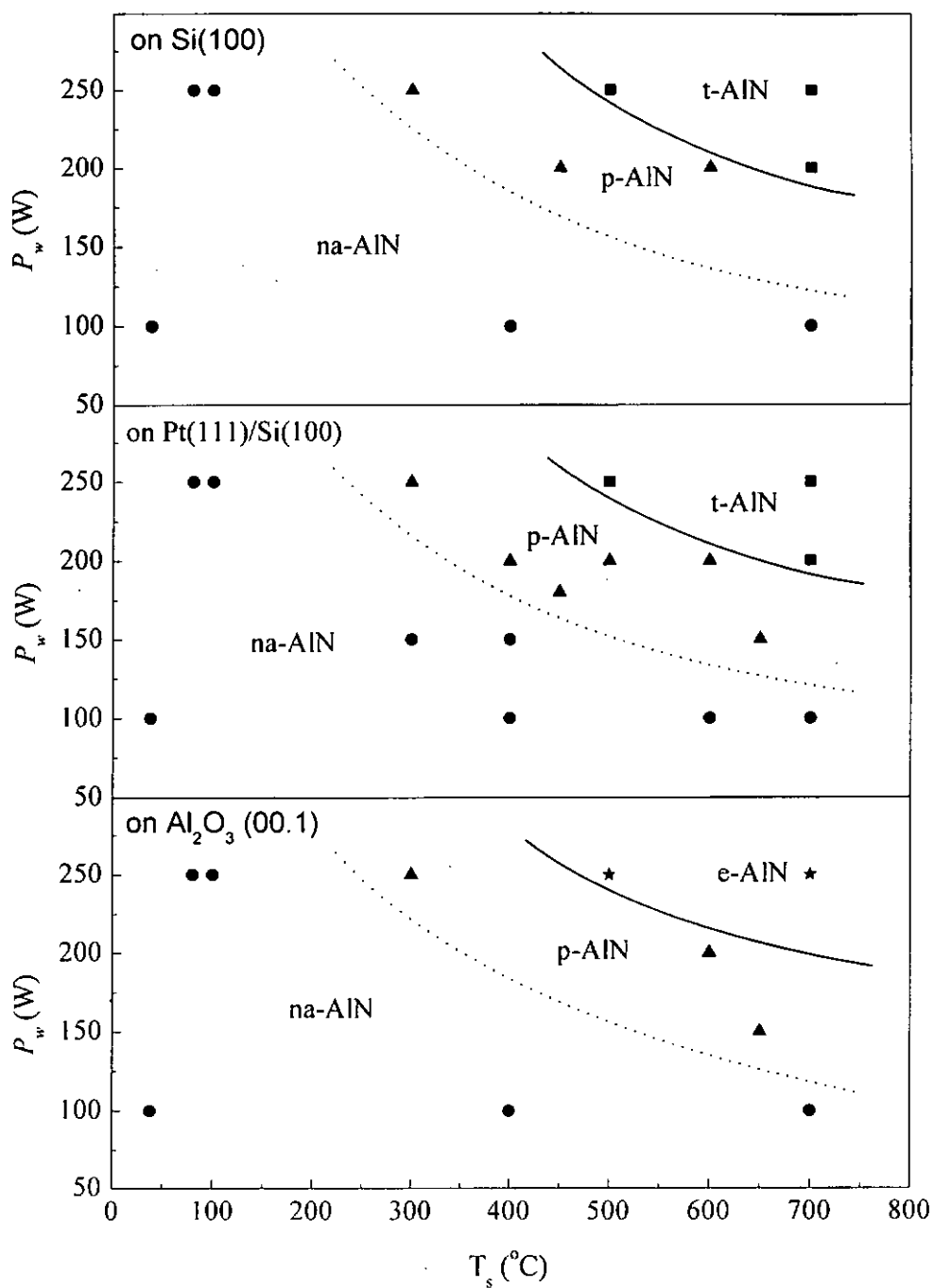


Fig. 3.11 T_s - P_w diagrams of AlN films deposited on (a) Si(100), (b) Pt(111)/Si(100) and (c) $Al_2O_3(00.1)$ substrates.



Fig. 3.11 (a) – (c) show that na-AlN films are formed with T_s or P_w , or both are set at low values. The location of the na-AlN region is independent on the substrate material used. When a set of T_s and P_w in the na-AlN region is used, the growth process is presumably dominated by a mechanism where the substrate material does not play any role to affect the arrangement of atoms on the substrate. This is why a high random network is detected for a na-AlN film according to the structural analysis.

In Fig. 3.11 (a), (b) and (c), all the p-AlN regions are located at moderate levels of T_s and P_w . The location of the p-AlN regions is independent on the substrate material used.

For the formation of a na-AlN film or a p-AlN film, the roles of T_s and P_w are apparently to be mutually compensated. The effect caused by the use of a lower T_s can be compensated by the use of a higher P_w , or vice versa.

Fig. 3.11 shows that for the films deposited on $\text{Al}_2\text{O}_3(00\cdot1)$ substrates, the e-AlN structure is formed at high T_s and P_w . However, at the same settings, the films deposited on Si(100) or Pt(111)/Si(100) are found to have the t-AlN structure instead.



In addition to T_s and P_w , some other parameters may also affect the film structure significantly. This poses an obstacle to reach a consensus on the parametric dependence of the AlN film structure experienced by different authors. For example, Cheng *et al* [Cheng, 2003] revealed that AlN films of preferential orientation could be obtained by using T_s of 350°C and P_w of 300 W. Referring to our T_s - P_w diagram, the same settings of T_s and P_w fall into the p-AlN region. One possible reason is that Cheng *et al* applied a shorter ratio of the target-to-substrate distance to the mean free path (D/p). The D/p that Cheng *et al* used was about 3.9, which was much smaller than 10 employed in our study. Therefore, in the present case, the species involved in the sputtering process experienced more severe scattering, such that their motions are highly randomized through frequent collisions. As explained before, this would cause a lower level of crystallization of the deposits. Iriarte *et al* used a D/p value as low as 2.5 to produce AlN films, which were found to have (00·1) texture, although the T_s they used was as low as 100°C. Okano *et al* also revealed that AlN films of preferential orientation could be produced by using D/p of 2 ~ 6, and at $T_s < 300^\circ\text{C}$. In order to have a unified understanding of all these findings, one has to take the effect of D/p into consideration. In general, the use of a small D/p value would lead to a film of high degree of crystallization and grain orientation.



3.4.2 Growth mechanisms

In this section, we discuss the growth mechanisms for the formation of different AlN film structures. Consider the na-AlN structure first. It is formed at low T_s and/or P_w . Obviously, at low setting of P_w , the plasma density generated above the target surface is lower. The average kinetic energy of the species generated in the plasma is also lower. In addition, the target-to-substrate distance (D) used in our experiments was 10 cm, which was longer than the mean free path (ρ) of the species in the vacuum of ≈ 5 mTorr. The mean free path of the species at a pressure of 5 mTorr is estimated to be about 1 cm. As such, the species would experience frequent collisions in the way of traveling towards the substrate. This enhances the random thermal motion of the particles. When they reach and land on the substrate surface, they are quite immobile and hence are condensed to form a rather disordered atomic network. The observation is consistent with what Lee *et al* [Lee, 1995] declare, that a AlN film of higher degree of crystallization can be obtained if the species involved are of large kinetic energies, and the mean free path is smaller. Even though a higher P_w is used, at such a low T_s , the species are still not energetically enough to give a good crystalline structure. The condensation of immobile species dominates the deposition process, so that the material of the substrate would not have significant influence on the film structure. Even the use of a $\text{Al}_2\text{O}_3(00\cdot1)$ substrate would not help to produce a film of crystalline structure.



For the formation of the p-AlN structure, moderate settings of T_s and P_w were used. It can be imagined that the settings of T_s and P_w in these ranges result in higher thermal energies of the species when they landed on the substrate surface. The setting of a high P_w increases the kinetic energy of the species involved in the sputtering process. Therefore, for the settings of T_s and P_w in the p-AlN region of a T_s - P_w diagram, the species landing on the substrate are more mobile and readily to form crystallites. Compared with the results of Kim *et al* [Kim, 1998], they claimed that AlN films grown at low temperature contain more voids. This was also explained by assuming that the species were immobile at this condition. Jagannadham *et al* reported that RMS AlN films deposited at T_s lower than 500°C are polycrystalline. At a higher T_s of 650°C, AlN films of (00·1) texture were produced. Lobel *et al* [Lobel, 2003] and Iriarte *et al* [Iriarte, 2002] claimed that AlN films deposited at higher T_s showed stronger preferential orientation. All these observations are consistent with what we observe for the p-AlN films deposited at relatively large T_s and P_w in the p-AlN region. We further suggest that the settings of T_s and P_w in the p-AlN region are not high enough to initiate strong preferential orientation of the AlN grains, but the grains are randomly oriented.



Films of the t-AlN and e-AlN structures were formed if higher T_s and P_w in the t- and e-AlN regions were used. High T_s renders the species to possess high thermal energy, and high P_w increases the kinetic energy of the species. As a result, the species are more readily to move around so as to arrange themselves to reach a lower energy state. The lower energy state is most likely to have an orderly crystalline structure, and so t- or e-AlN structures are more readily formed.

Under this situation, the film formation process is not dominated by “quick condensation” of immobile species like the cases at low T_s and/or P_w , but the selection of the substrate material would be expected to give significant influence on the film structure. In particular, $\text{Al}_2\text{O}_3(00\cdot1)$ substrates used in our case would be more favourable for the formation of the e-AlN structure. Furthermore, with the use of the same high levels of T_s and P_w , the films deposited on other substrates like Si(100) or Pt(111)/Si(100) can only have the t-AlN structure.

Zhang *et al* [Zhang, 1994] pointed out that there is a 12.2% lattice mismatch between AlN(00·1) and Pt(111). Sun *et al* [Sun, 1994] reported a 13.29% lattice mismatch between AlN(00·1) and $\text{Al}_2\text{O}_3(00\cdot1)$. For example, the latter case is depicted in Fig. 3.8.



Fig. 3.8 shows the top view of the epitaxial relationship between AlN(00·1) and Al₂O₃(00·1). The thick solid lines represent the unit cells of AlN and Al₂O₃. In this type of matching, AlN [10·0] and Al₂O₃ [$1\bar{1}$ ·0] are along the same direction. The lattice mismatch is equal to the difference between the Al-Al bond lengths in the AlN and Al₂O₃ substrates. The Al-Al bond length of AlN (d') is 0.311, nm whereas that of Al₂O₃ (d) is 0.274 nm. The lattice mismatch can be calculated as $\frac{d' - d}{d} = 13.3\%$. Therefore, the lattice matching between the AlN film and the Al₂O₃(00·1) substrate is not quite perfect.



3.5 Structural information revealed by IR absorption

IR absorption data provide more structural information of the films. The infrared absorption spectra of some typical AlN films deposited on Si(100) are shown in Fig. 3.12.

For a na-AlN film, the spectrum exhibits a very broad absorption band covering the wavenumber range from $600 - 700 \text{ cm}^{-1}$. This band covers the positions of many absorption bands of the bulk crystalline AlN. From the XRD data, we suggest that the na-AlN structure consisting of a highly disordered matrix in which many small grains are embedded. Now, the IR data seems to support this conjecture. The broad IR absorption band could come from the AlN grains or from the matrix. Both of these structures retain the short range order analogous to that of the crystalline AlN structure. The whole film structure is so disordered, such that there are variations of bond length and bond angle between the atoms. This explains the broadness of the IR peak observed.

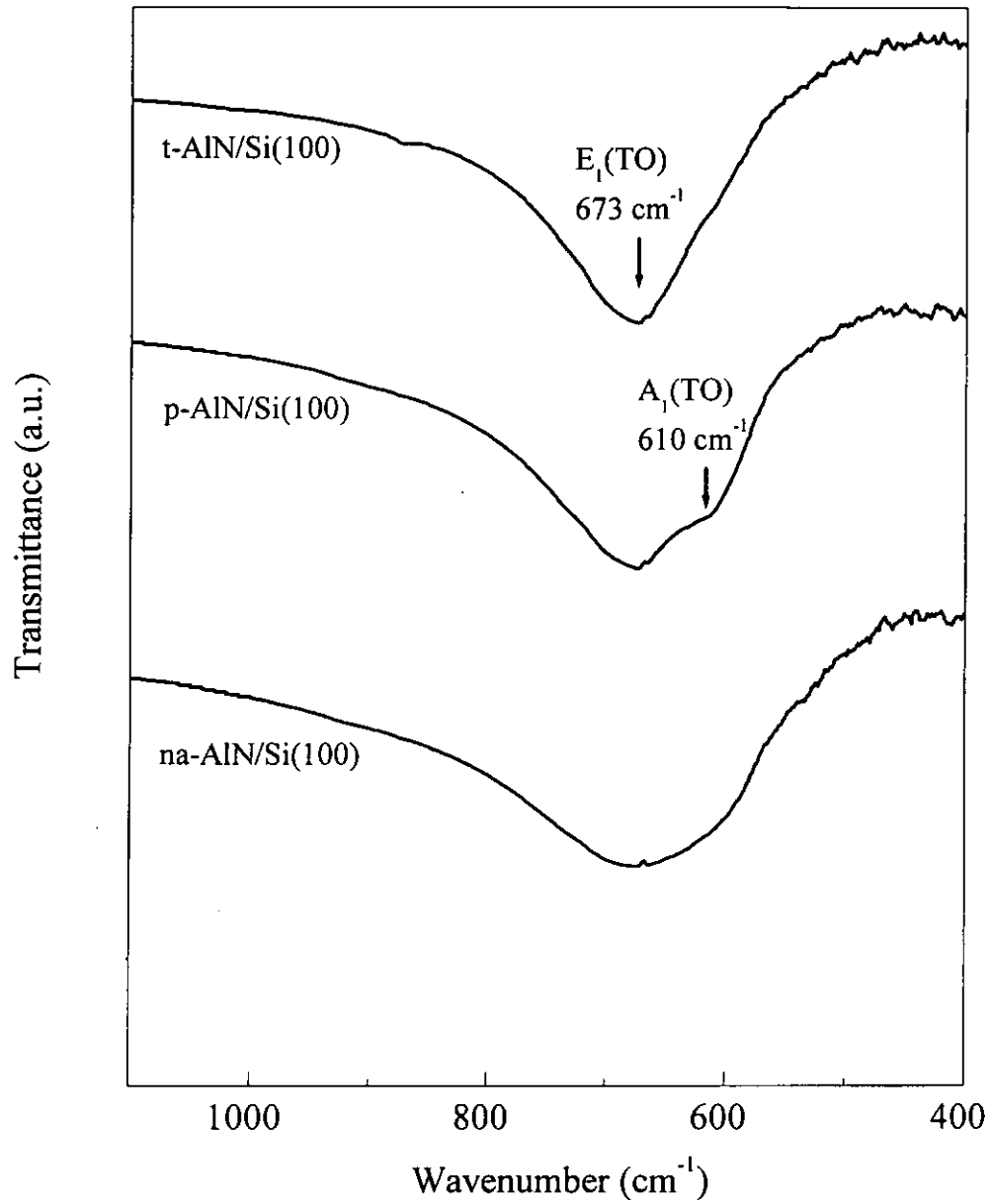


Fig. 3.12 Typical IR absorption spectra of na-AlN, p-AlN and t-AlN films deposited on Si(100) substrates.



Fig. 3.12 shows some subtle features of the IR absorption spectrum of a p-AlN film. The spectrum still contains a broad absorption band, but showing a shoulder at 610 cm^{-1} . The dip of the main peak is at 673 cm^{-1} . The dip and the shoulder can be associated with the transverse $E_1(\text{TO})$ and $A_1(\text{TO})$ modes of the crystalline AlN structure. Further explanation is shown in Fig 3.13 (a) and (b). Fig. 3.13 (a) depicts the situation when the electrical field of the incident infrared beam is in parallel with the c-axis of the grains, where the c-axes of the grains are aligned in parallel to the substrate surface. The E-field interacts with the grains to excite the $E_1(\text{TO})$ mode vibration (Fig 3.13 (a)). Fig. 3.13 (b) depicts the case where the electric field of the incident IR beam is in perpendicular to the c-axes of the grains, with the c-axes aligned in perpendicular to the substrate surface. The IR radiation excites the $A_1(\text{TO})$ mode vibration under this configuration (Fig 3.13 (b)). The two types of vibrations contribute to the generation of the observed main IR peak and the small shoulder.

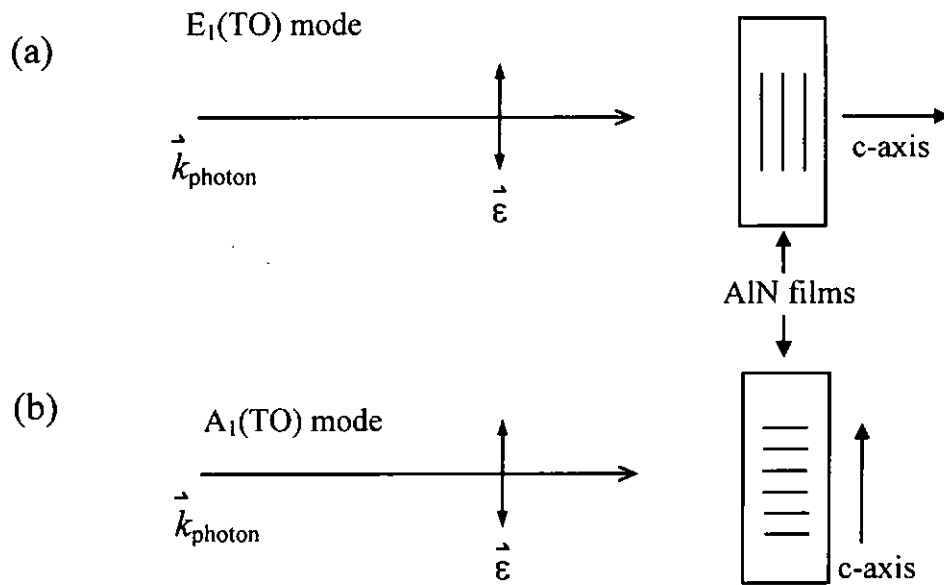


Fig. 3.13 Schematic diagrams showing the generation of (a) $E_1(\text{TO})$ mode and (b) $A_1(\text{TO})$ mode of an AlN film in an IR absorption experiment.

It is mentioned before that the $E_1(\text{TO})$ phonon mode is mainly excited when most of the grains are aligned with their c-axis in perpendicular to the film surface. Our t-AlN films have this features, so that the IR spectrum is dominated by the absorption band of the $E_1(\text{TO})$ mode (673 cm^{-1}). For a t-AlN film of even more orderly c-axis alignment, only the absorption band of the $E_1(\text{TO})$ mode is seen, but that of the $A_1(\text{TO})$ mode becomes very weak. The case for a na-AlN film is at another extreme, as the structure is extremely random, so that IR absorption band shows the join contribution from both of the vibrational modes. It appears to be broad, since it covers the ranges of the two vibrational modes.



We noted that other authors also claimed the observations of the IR absorption peaks associated with the $E_1(\text{TO})$ mode and $A_1(\text{TO})$ mode (Table 3.14). Wei *et al* [Wei, 1997] reported a peak of the $E_1(\text{TO})$ mode at 668 cm^{-1} . McNeil *et al* [McNeil, 1993] reported a peak of the $E_1(\text{TO})$ mode at 673 cm^{-1} . McNeil *et al* and Perlin *et al* [Perlin, 1993] reported a peak of the $A_1(\text{TO})$ mode at 614 cm^{-1} and 607 cm^{-1} , respectively. The positions of the IR peaks observed in the present study consistent quite well with these results. Finally, we point out that the spectrum is very broad, so that it should contain the contributions from other phonon modes, such as $A_1(\text{LO})$ mode at 663 cm^{-1} reported by Carlone *et al* [Carlone, 1984].

$A_1(\text{TO})$ mode	$E_1(\text{TO})$ mode	Reference
607 cm^{-1}	--	Perlin <i>et al</i>
--	668 cm^{-1}	Wei <i>et al</i>
614 cm^{-1}	673 cm^{-1}	McNeil <i>et al</i>
610 cm^{-1}	673 cm^{-1}	Present work

Table 3.14 AlN optical phonon frequencies at different modes.



3.6 Oxygen contamination

Since our chamber cannot reach the ultrahigh vacuum condition, therefore some oxygen-containing residual species may exist. They may be incorporated into the deposits to cause oxygen contamination. In the worst case, the formation of the AlN structure could be prohibited due to the high concentration of impurities. To prevent from this situation to happen, Dubois *et al* [Dubois, 1999] used a vacuum system capable of reaching a pressure below 10^{-7} Torr, in order to avoid oxygen contamination of AlN films. Jagannadham *et al* [Jagannadham, 1998] even suggested that good vacuum with an ultimate pressure $< 10^{-7}$ Torr is quite necessary in order to deposit high quality AlN films. In this work, no IR absorption associated with the vibrational mode of Al-O bond at 460 cm^{-1} [Nyquist, 1971] and O-H bond at the range of $3900\text{--}3400\text{ cm}^{-1}$ [Tait, 2001] were observed. This suggests that the oxygen content in the films is negligibly small. Since our system is not an ultrahigh vacuum system, we suggest that the condition of ultrahigh vacuum may not be so important for the growth of AlN films with texture and epitaxial structures.



Chapter 4

Structure dependence of the properties of AlN Films

4.1. Piezoelectric properties

In this section, the piezoelectric properties of AlN films with different crystallographic structures are presented and discussed. The piezoelectric properties of the films are mainly represented by their piezoelectric coefficient d_{33} .

4.1.1 Comparison of piezoelectric signals collected by using a lock-in amplifier and a spectrum analyzer

The piezoelectric coefficients d_{33} of AlN films were measured by using laser interferometer technique. In a measurement, an a.c. voltage was applied to the electrodes made on the two sides of a film in the configuration of a parallel plate capacitor. The frequency of the applied field was 15 kHz. The piezoelectric signal generated from the sample was collected simultaneously by using a lock-in amplifier and a spectrum analyzer. The results of d_{33} values measured from the signals displayed by the two instruments were compared in the section.





Fig. 4.1 shows that the difference of the d_{33} values calculated from the signals detected by the lock-in amplifier and the spectrum analyzer. The d_{33} values measured by the two instruments are 2.0 pm V^{-1} and 2.6 pm V^{-1} , respectively. The measurement involves the determination of a very small displacement, so the performance of the measuring instrument influences significantly the reliability and accuracy of the result.

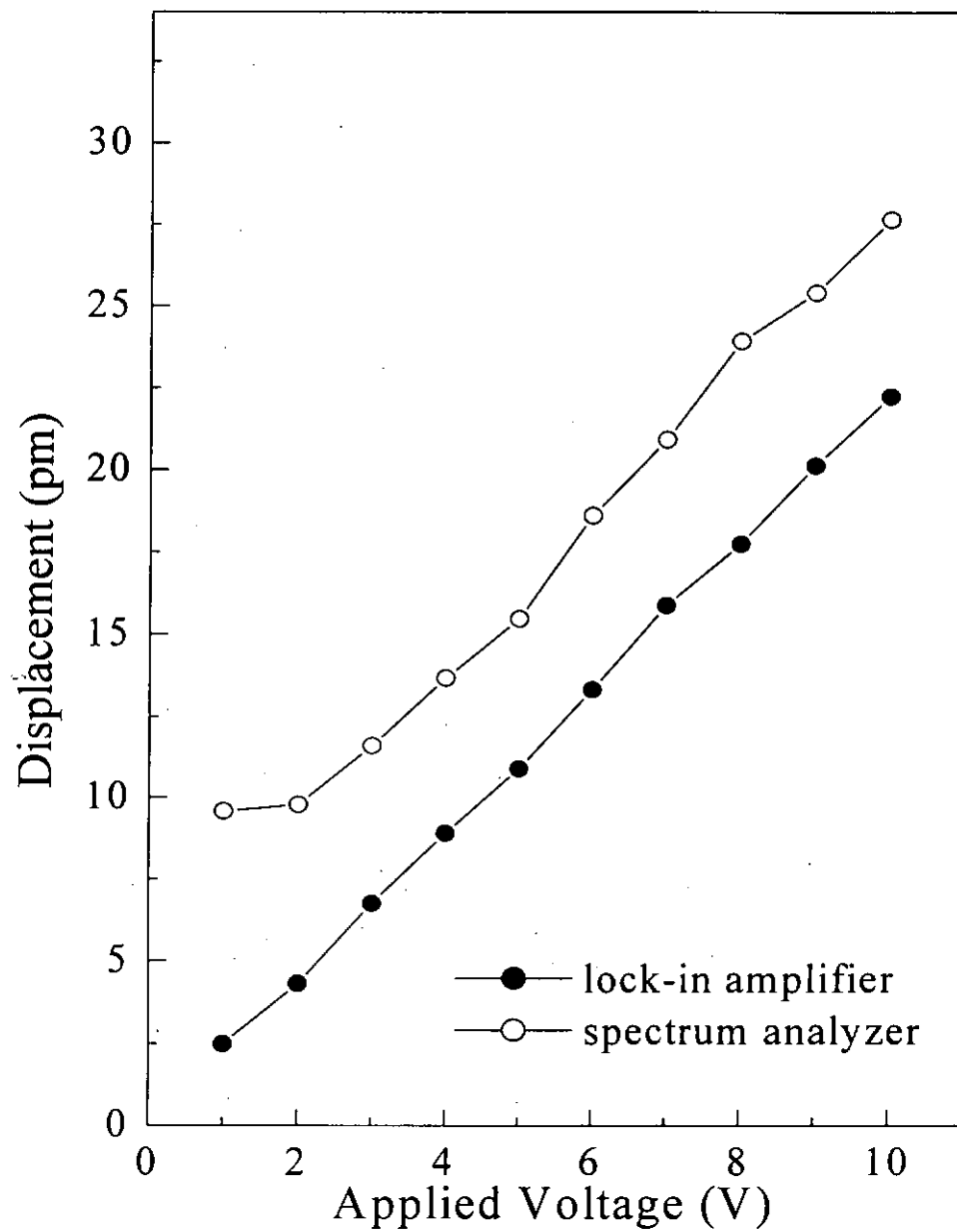


Fig. 4.1 The displacement of the piezoelectric effect of AlN film as a function of applied voltage measured by a lock-in amplifier and a spectrum analyzer.



Compared with the data measured by a spectrum analyzer, the data recorded by using a lock-in amplifier show a more linear dependence on the applied voltage (Fig. 4.1). In addition, lock-in amplifier is powerful in removing the random noise, and so is more favorable to achieve a much better signal-to-noise ratio. Third, the linear extrapolation of the data approximately passes through the origin. On the contrary, the data obtained by using a spectrum analyzer show inferior linear dependence on the applied voltage, and are more fluctuating. Their linear extrapolating does not pass through the origin. Consequently, the data recorded by using a lock-in amplifier are believed to be more reliable and are used for the analyses.



4.1.2 Uniformity of d_{33} value

The uniformity of d_{33} at different positions on the film surface was investigated. Fig. 4.2 shows the results of measurements measured at three different positions on the film surface. The deviations between the results of the measurements are small. The measured displacement depends linearly on the input voltage remains linear even when the voltage is increased to 10 V. The three d_{33} values extracted from the curves fall in a range of $2.5 - 3.0 \text{ pm V}^{-1}$. The small deviation of the results shows that the piezoelectric properties of a film are quite uniform throughout the whole sample.

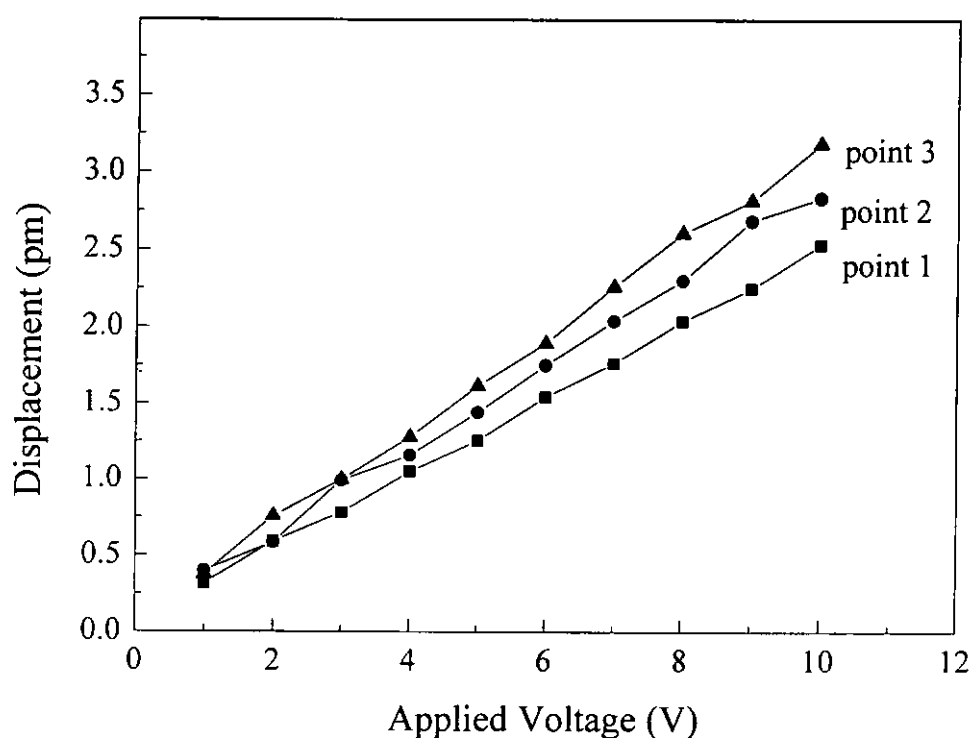
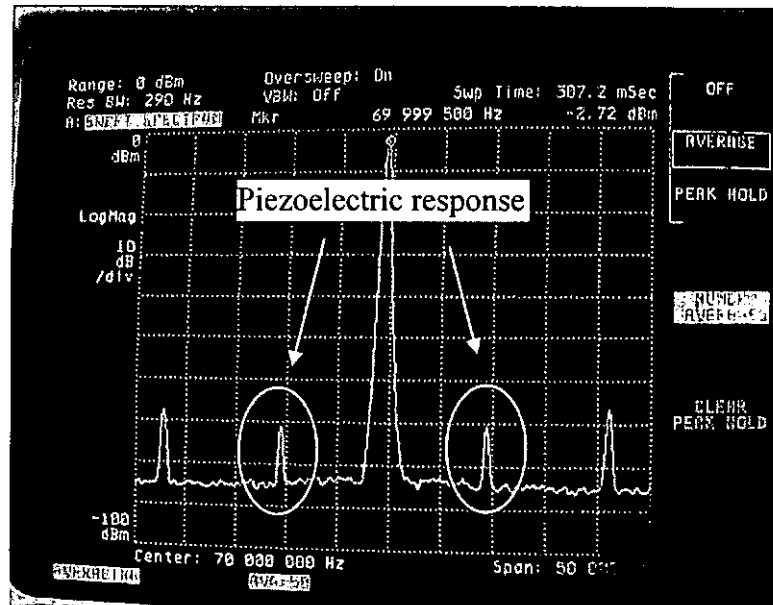


Fig. 4.2 Displacement vs. applied voltage measured at different positions on an AlN film.



To identify a true signal, one may refer to the spectrum displayed by a spectrum analyzer. If a peak (Fig. 4.3) is a true signal caused by the piezoelectric response of the film, its position (frequency) would be changed coherently with the change in the frequency of the excitation voltage. For example, Fig. 4.3 shows that when the frequency of the excitation voltage generated by a function generator was 10 kHz, two small peaks appeared at ± 10 kHz from a central peak at 70 MHz (operation frequency of the Bragg cell). When the excitation frequency was changed to 15 kHz, the positions of the two small peaks shifted to ± 15 kHz from the central peak. With this coherent change, the two small peaks were thus identified to be the true piezoelectric signals of the sample, but not from the background noise.

(a)



(b)

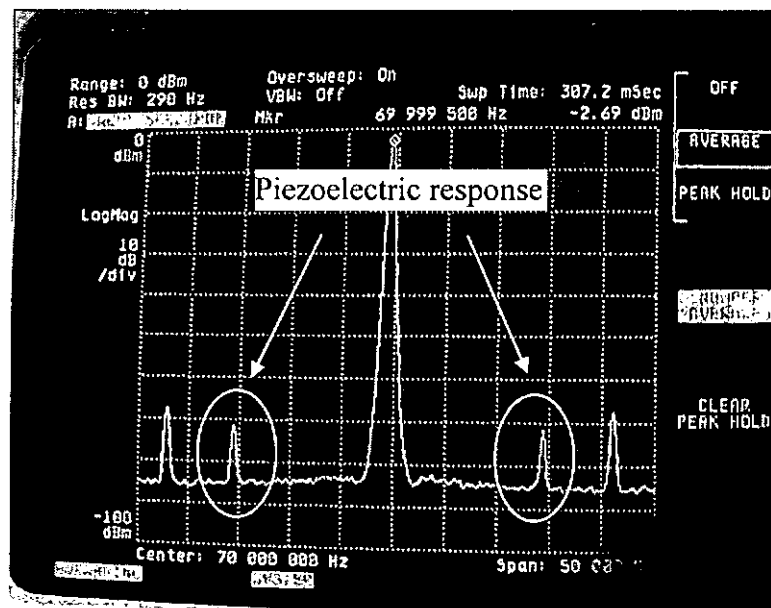


Fig. 4.3 The piezoelectric responses of an AlN film displayed by a spectrum analyzer with a input voltage at frequencies of (a) 10 kHz and (b) 15 kHz.



4.1.3 Correction of clamping effect

Since all of the AlN films used for d_{33} measurements are deposited on Pt(111)/Si(100) substrates, so the presence of the substrates would pose additional constrain to the piezoelectric deformation of films during measurements. This is termed as the clamping effect. The apparent d_{33} value measured should be smaller than the true value. Correction is therefore necessary to obtain the true d_{33} value of the film. According to Lueng *et al* [Lueng, 2000], the true piezoelectric coefficient of a free-standing film denoted by (d'_{33}) can be calculated from the measured d_{33} value according to the formula:

$$d_{33} = d'_{33} - 2\left(\frac{d'_{31}S^E_{13}}{S^E_{11} + S^E_{12}}\right) \dots\dots\dots(4.1.1)$$

where $d'_{31} \cong -\frac{d'_{33}}{2}$ is another component of the piezoelectric coefficients of the unclamped film sample, and S^E_{ij} ($j = 1, 2$ and 3) are the elastic compliances of the sample. The compliance data calculated by using the Hartree-Rock theory are compiled by Ruiz *et al* [Ruiz, 1994], i.e. S^E_{11} , S^E_{12} and $S^E_{13} = 2.5 \times 10^{-12}$, -0.7×10^{-12} and $-0.5 \times 10^{-12} \text{ m}^2\text{N}^{-1}$, respectively. For a measured d_{33} value of 4.0 pm V^{-1} for a t-AlN film, the corrected d'_{33} value is 5.5 pm V^{-1} . d_{33} shows a percentage error of 30% compared to the true value d'_{33} . Due to the significance of the substrate clamping effect as shown, the piezoelectric coefficients presented in the following have been collected according to equation (4.1.1).



4.1.4 Structure dependence of the piezoelectric effect of AlN films

One may image that the piezoelectric coefficient of an AlN film would be affected by its crystallographic structure (including the grain size and orientation). In this section, we report and discuss how the piezoelectric properties of the film samples depend on the microstructures of our AlN films as described in Chapter 3. Five samples, having na-AlN, p-AlN and t-AlN structures were selected for investigations. Their preparation conditions are listed in Table 4.4.

Sample no.	T_s	P_w	thickness	structure
AlN#44	100°C	100 W	0.5 μm	na-AlN
AlN#32	480°C	200 W	1 μm	p-AlN
AlN#34	500°C	200 W	1 μm	p-AlN
AlN#40	500°C	180 W	0.7 μm	p-AlN
AlN#57	700°C	250 W	0.5 μm	t-AlN

Table 4.4 The deposition conditions and thickness of AlN films with different structures for piezoelectric measurements.

na-AlN

Up to date, most of the investigations on the piezoelectric properties of thin films were conducted on crystalline samples. Little reports have been made to report the piezoelectric properties of disordered AlN films. In this section, we describe the results of the measurements of the piezoelectric properties of our na-AlN films.

Fig. 4.5 shows the plot of the displacement vs. the magnitude of the voltage applied to sample AlN#44. This sample was fabricated at $T_s = 100^\circ\text{C}$ and $P_w = 100\text{ W}$ (Table 4.4), and was confirmed to have the na-AlN structure. The film thickness was about $0.5\text{ }\mu\text{m}$. As shown in Fig. 4.5, the piezoelectric displacement depends linearly on the driving voltage at a frequency of 15 kHz . The correlation coefficient of the linear best fit is 0.99891 . The d_{33} value of this na-AlN made on Pt(111)/Si(100) is determined to be $d_{33} = 0.2\text{ pm V}^{-1}$. After correction, the d'_{33} value $= 0.28\text{ pm V}^{-1}$. This result reveals that an AlN film consisting of a highly disordered atomic network can also exhibit a detectable piezoelectric coefficient.

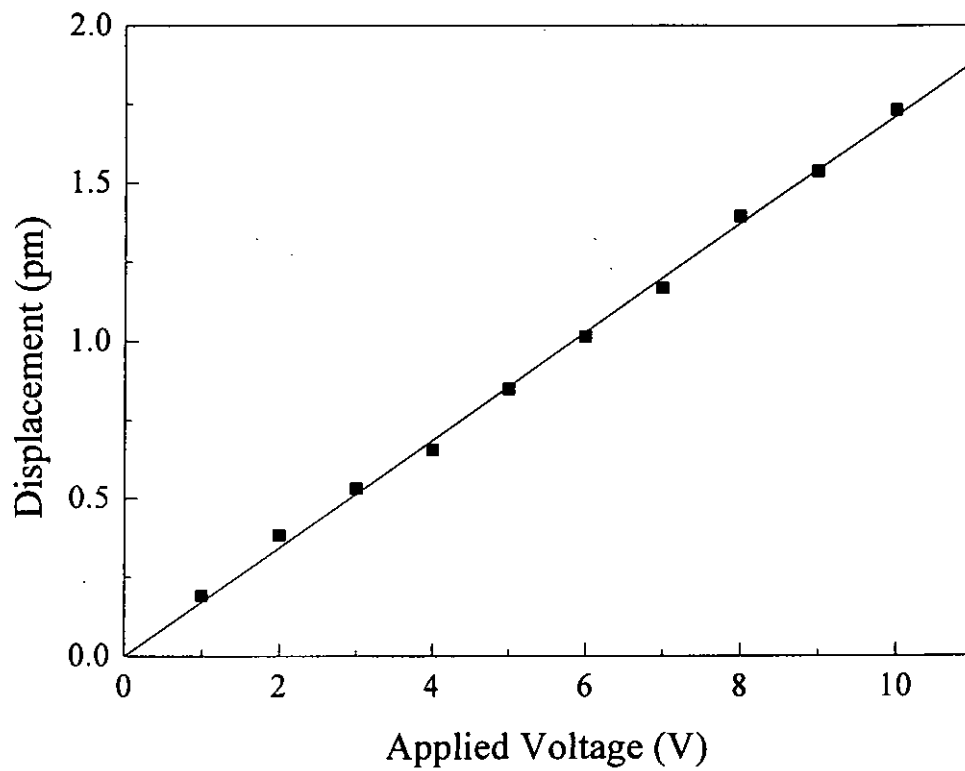


Fig. 4.5 A plot of displacement vs. applied voltage for a na-AlN film (AlN#44).



p-AlN

It is expected that the piezoelectric response of a p-AlN film would be greater than that of a na-AlN film. Fig. 4.6 (a) and (b) show the displacement of two p-AlN films, (AlN#32 and AlN#34) as a function of the applied voltage. They were deposited at $T_s = 480 - 500^\circ\text{C}$ and $P_w = 200 \text{ W}$ in the p-AlN region of the T_s - P_w diagram (Fig. 3.10). The piezoelectric displacement responses linearly with the applied voltage (15 kHz), and the correlation coefficient of the best linear fit is 0.99987. The d_{33} values of the two p-AlN films were determined to be 1 pm V^{-1} . After correction, the d'_{33} value is calculated to be 1.3 pm V^{-1} .



More complication was found for a third p-AlN film fabricated at similar conditions, i.e. AlN#40 (Table 4.4). The plot of the displacement against the applied voltage is shown in Fig. 4.7. The data show very good linearity with a correlation coefficient of 0.99977. The d_{33} value of this sample is 4.5 pm V^{-1} ($d'_{33} = 6.2 \text{ pm V}^{-1}$), which is much greater than those of other two p-AlN films described above. This is not clear why the d'_{33} value of this p-AlN would have such a great deviation from that of the other two. Perhaps the size or grain orientation of this AlN#40 is not the same as those of the other two samples, whereas the piezoelectric properties of a polycrystalline AlN films are very sensitive to the grain size and orientation. The results described in this section lead us to conclude that, on average, the d_{33} value of a p-AlN film is prominently larger than that of na-AlN film. Further support came from Guy [Guy, 1999], who revealed that polycrystalline AlN films grown at 90°C and 200°C had d_{33} values of 3.2 pm V^{-1} and 4.0 pm V^{-1} , respectively. The piezoelectric response of a more porous AlN films was found to drop significantly. This explains why the piezoelectric coefficient of our na-AlN films is much smaller than those of the p-AlN and t-AlN samples.

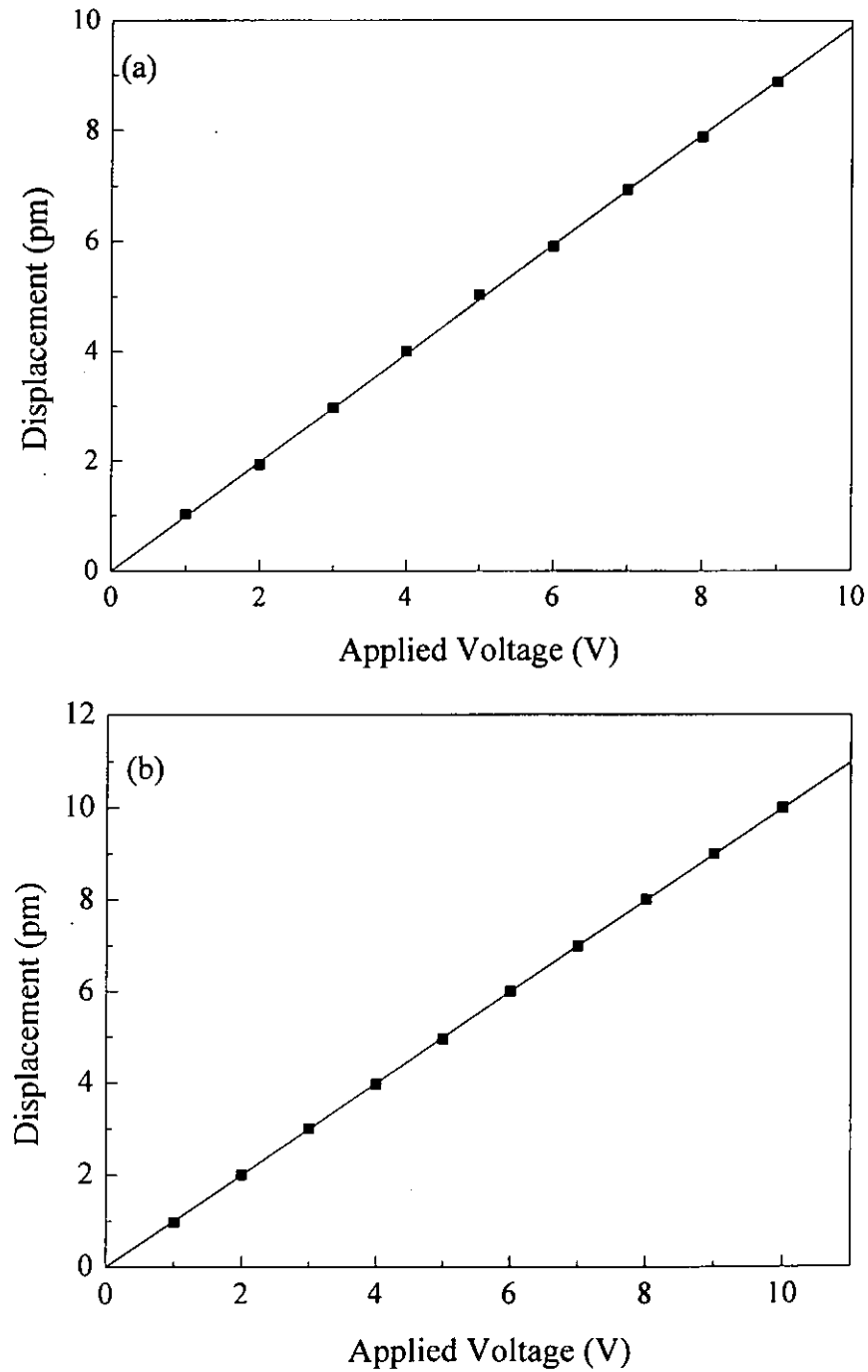


Fig. 4.6 Plots of displacement vs. applied voltage for two p-AlN films (a) AlN#32 and (b) AlN#34.

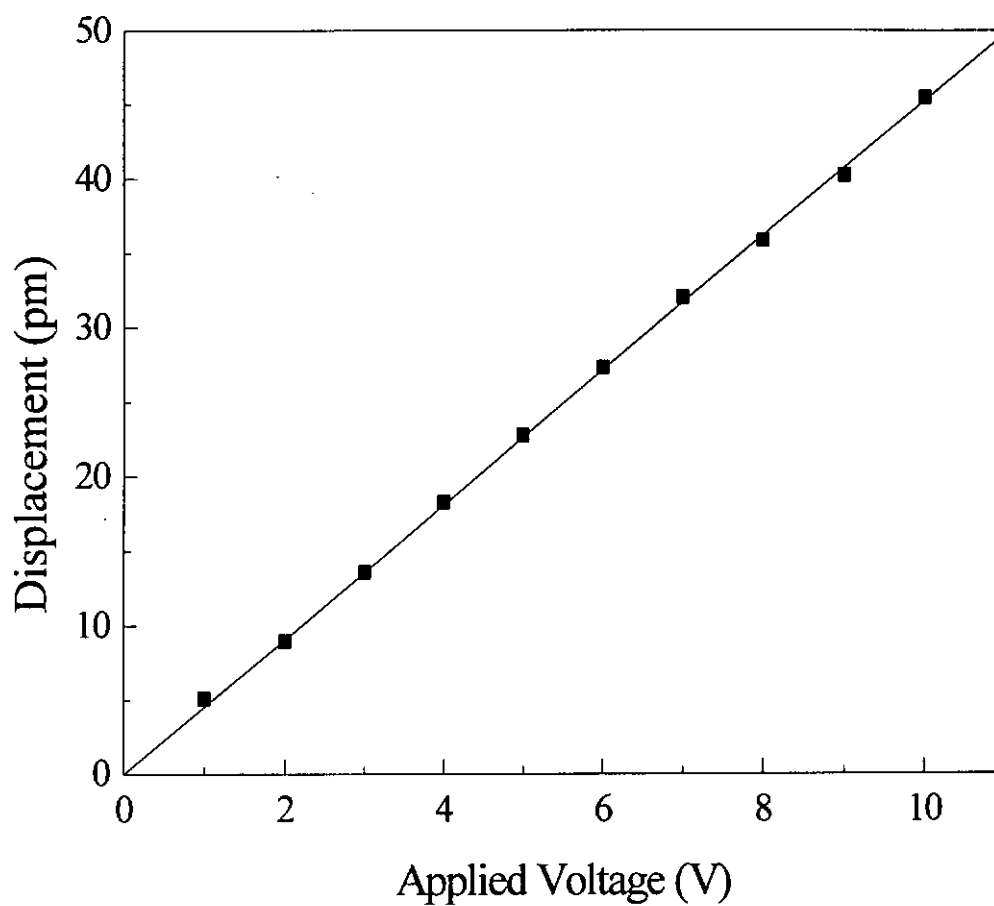


Fig. 4.7 Surface displacement of AlN#40 as a function of applied voltage.

t-AlN

Fig. 4.8 shows the surface displacement as a function of applied voltage for a t-AlN film (AlN#57). The piezoelectric displacement also shows linear dependence on the applied voltage (15 kHz). The correlation coefficient of the best linear fit is 0.98345. The d_{33} value of the film extracted from the slope of the fitting line is $d_{33} = 4.0 \text{ pm V}^{-1}$ ($d'_{33} = 5.5 \text{ pm V}^{-1}$).

This value is quite consistent with some previously reported data. For example, Lueng *et al* reported a piezoelectric coefficient of 3.9 pm V^{-1} for epitaxial AlN films prepared by MBE technique, which is quite close to our present result. Finally, we point out that this is not the true piezoelectric coefficient of the film.

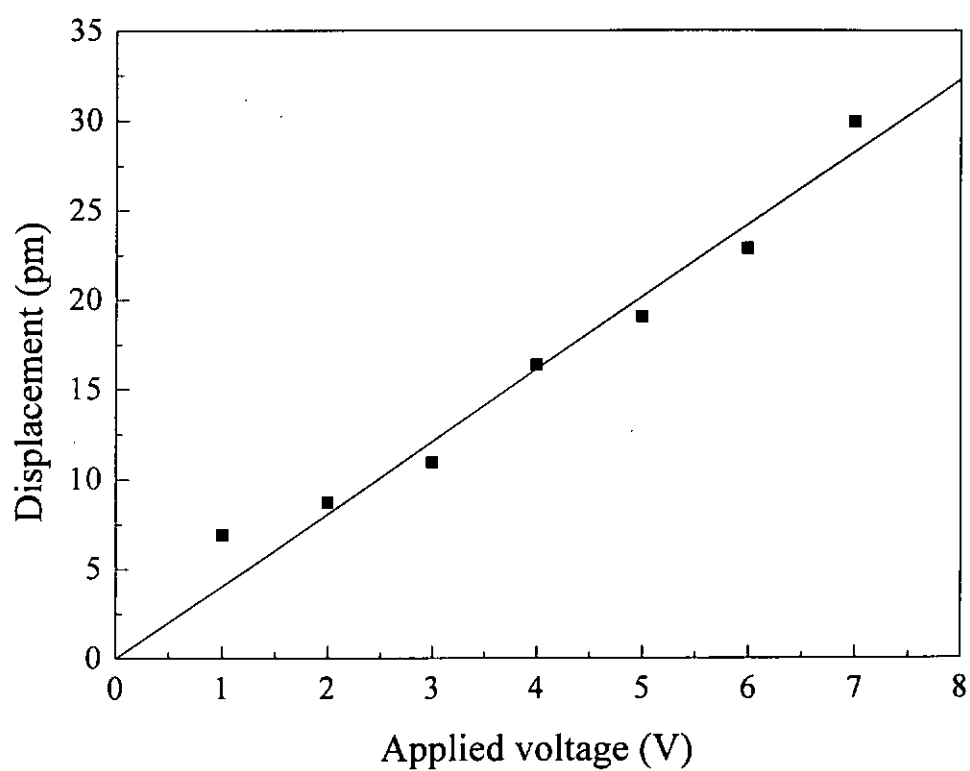


Fig. 4.8 Surface displacement for sample AlN#57 as a function of the applied voltage.



Fig. 4.9 summarizes the comparison of the d'_{33} values of the AlN films having different structures. The d'_{33} of the na-AlN film was the lowest (0.28 pm V^{-1}). From the results, we verify that a highly disordered AlN film can also have detectable piezoelectric effect. The magnitude of the piezoelectric effect of a na-AlN film is about 20 times lower than that of a p- or t-AlN film ($\approx 5.5 - 6 \text{ pm V}^{-1}$). The values of d'_{33} of p-AlN films are larger and vary in a broad range from 1.3 to 6.2 pm V^{-1} . This is possibly because the p-AlN films can have different grain size and orientation, which can affect significantly the piezoelectric response of the films. The d'_{33} value of the t-AlN film is $\approx 5.5 \text{ pm V}^{-1}$, which is approximately equal to the upper bound of the range for the p-AlN films.

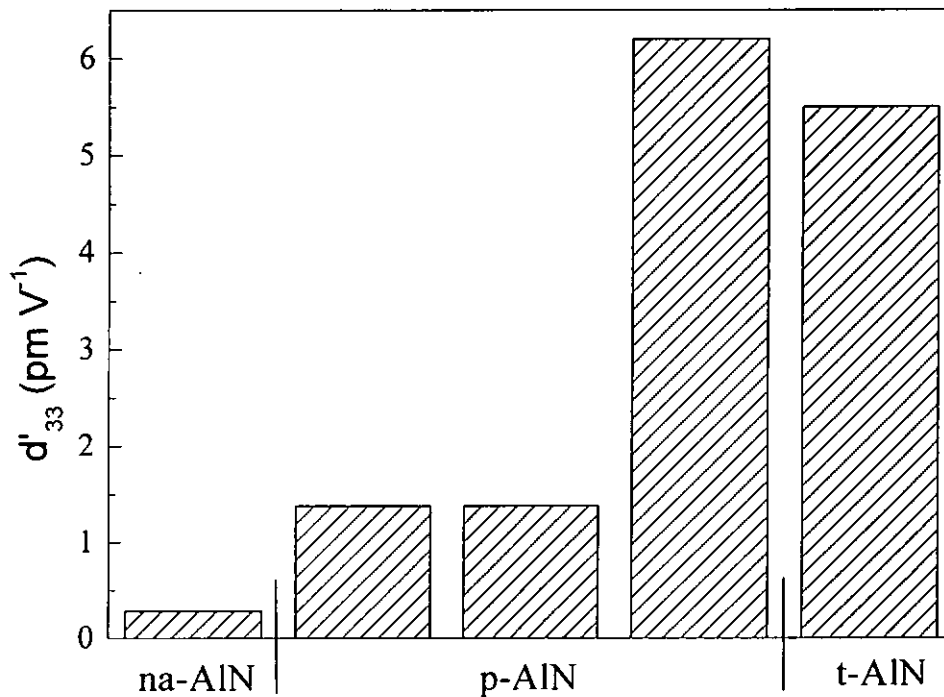


Fig. 4.9 d'_{33} values of AlN films with different structures.



4.2 Dielectric properties

The capacitances of three p-AlN films deposited on Pt(111)/Si(100) substrate were measured at a low frequency range of 10 kHz – 1 MHz, from which the dielectric properties in this frequency range were calculated. The capacitances measured in this frequency range are shown in Fig. 4.10. The data of the films with other structures were not obtained, because the top electrodes were easily damaged in the process of wire bonding.

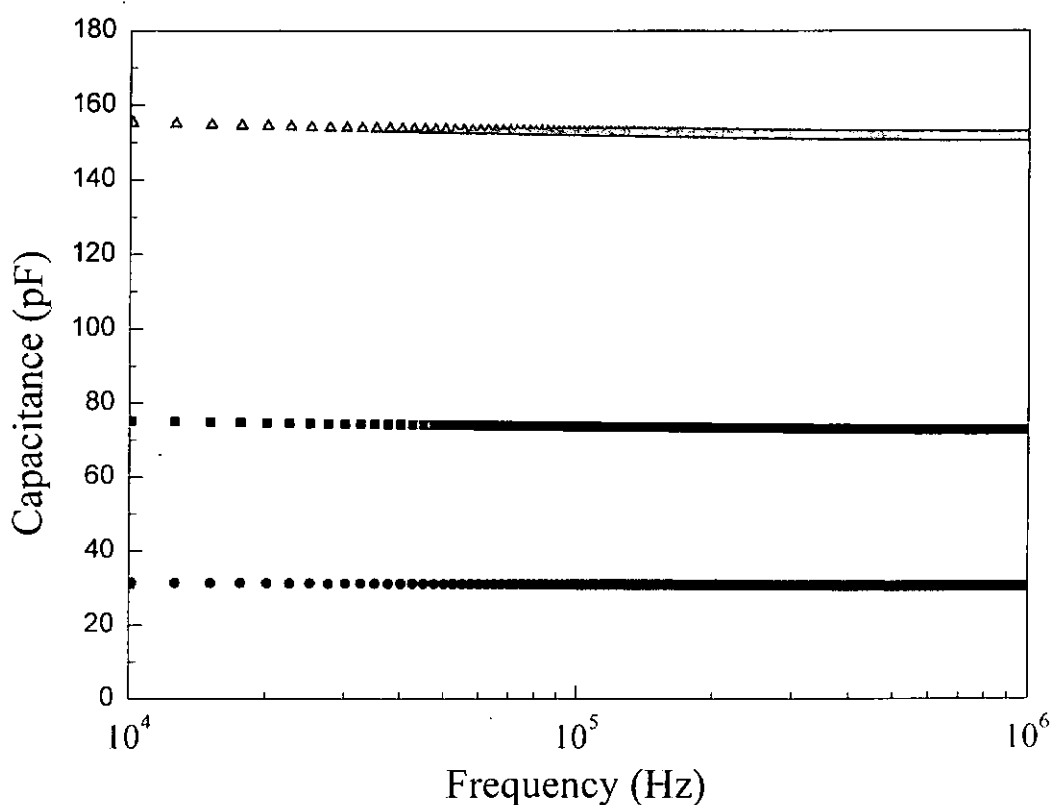


Fig. 4.10 Capacitance of AlN films in the frequency range of 10 kHz – 1 MHz.



The capacitances of the three AlN films deposited at similar conditions are almost independent on frequency in the range of 10 kHz – 1 MHz. The values of the capacitance fall in the range of 30 – 160 pF. From the equation $C = \frac{\epsilon\epsilon_0 A}{d}$ [referred to Chapter 2], the dielectric constants ϵ was calculated and plotted in Fig. 4.11 (a). The range of the dielectric constants of AlN films is between 9 – 13. Fig. 4.11 (b) shows the dielectric loss of the films, which lies in the range of 0.01 – 0.15.

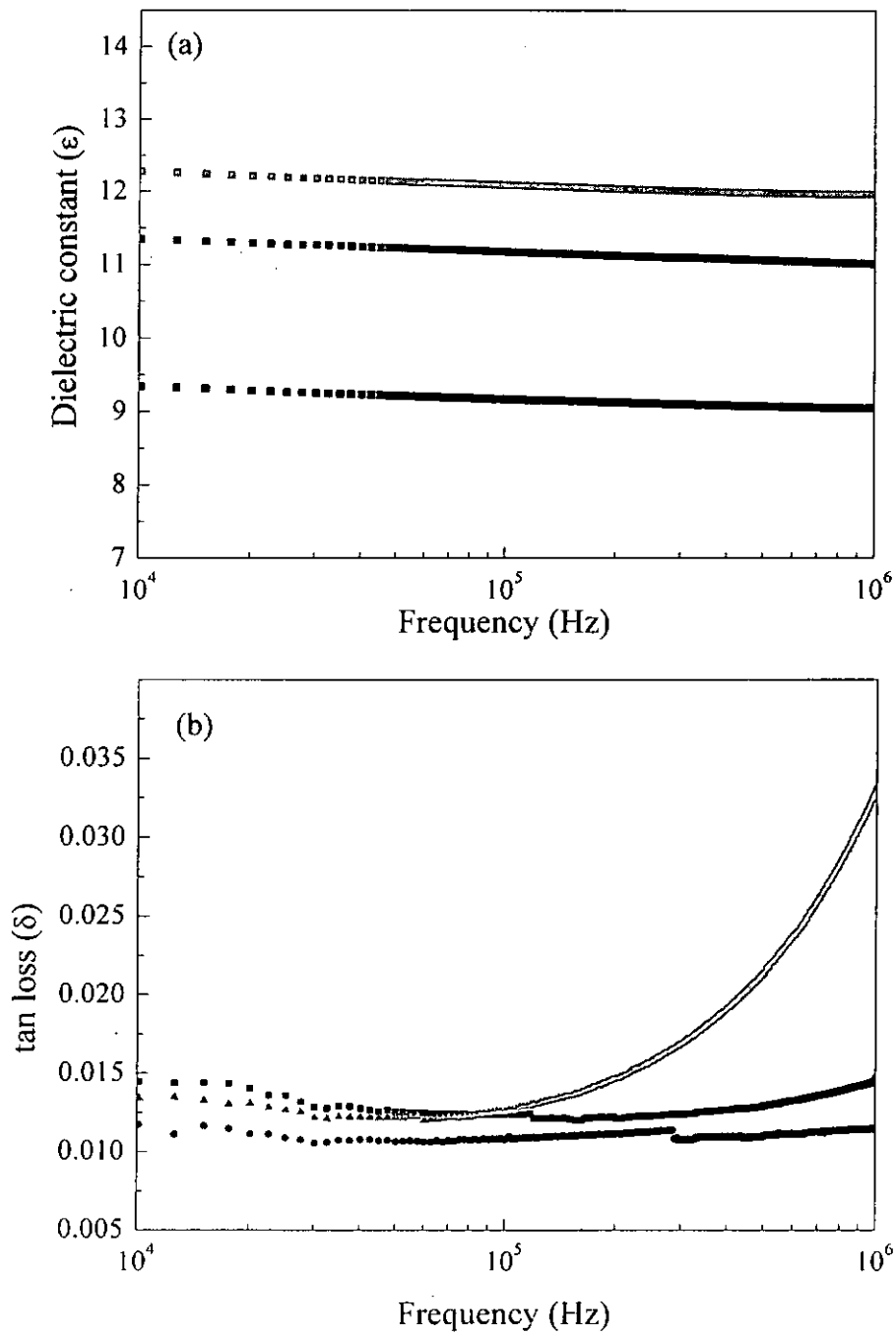


Fig. 4.11 (a) Dielectric constants and (b) tangent loss of AlN films in the frequency range of 10 kHz – 1 MHz.



4.3 Mechanical properties

In this section, we present the results of the measurements of the hardness (H) and young's modulus (E) measurements of the AlN films deposited on Si(100) substrates as functions of the AlN structure.

4.3.1 Indentation depth dependence of hardness and young's modulus

Fig 4.12 (a) and (b) show the hardness (H) and young's modulus (E) of the AlN films as functions of penetration depth. With increasing penetration depth, both the measured H and E rise with increasing depth. Both of them reach a peak values, and then drop to a plateaus. The initial rise of the data with depth could be due to the fact that the deformation of the indented point is still completely elastic. On the other hand, the drop of the H and E data at deeper penetration depths > 300 nm is caused by the influence coming from the substrate deformation. In order to get the true mechanical properties of the film material, we referred to the rule of thumb widely used in the past, which states that the substrate effect can be neglected if the indentation depth of a test is below 1/10 of the film thickness (≈ 50 nm). At this range of depth, the deformation of the substrate is small, so it would not affect significantly to the results of measurements. Looking at the data of Fig. 4.12 as an example, the film hardness is determined to be ≈ 20 GPa, which is extracted from that data corresponding to the data collected at depths of about 1/10 of the film thickness. The



corresponding E value is 250 GPa. The H and E values measured at a penetration depth of 1000 nm are very close to those of the Si(100) substrate.

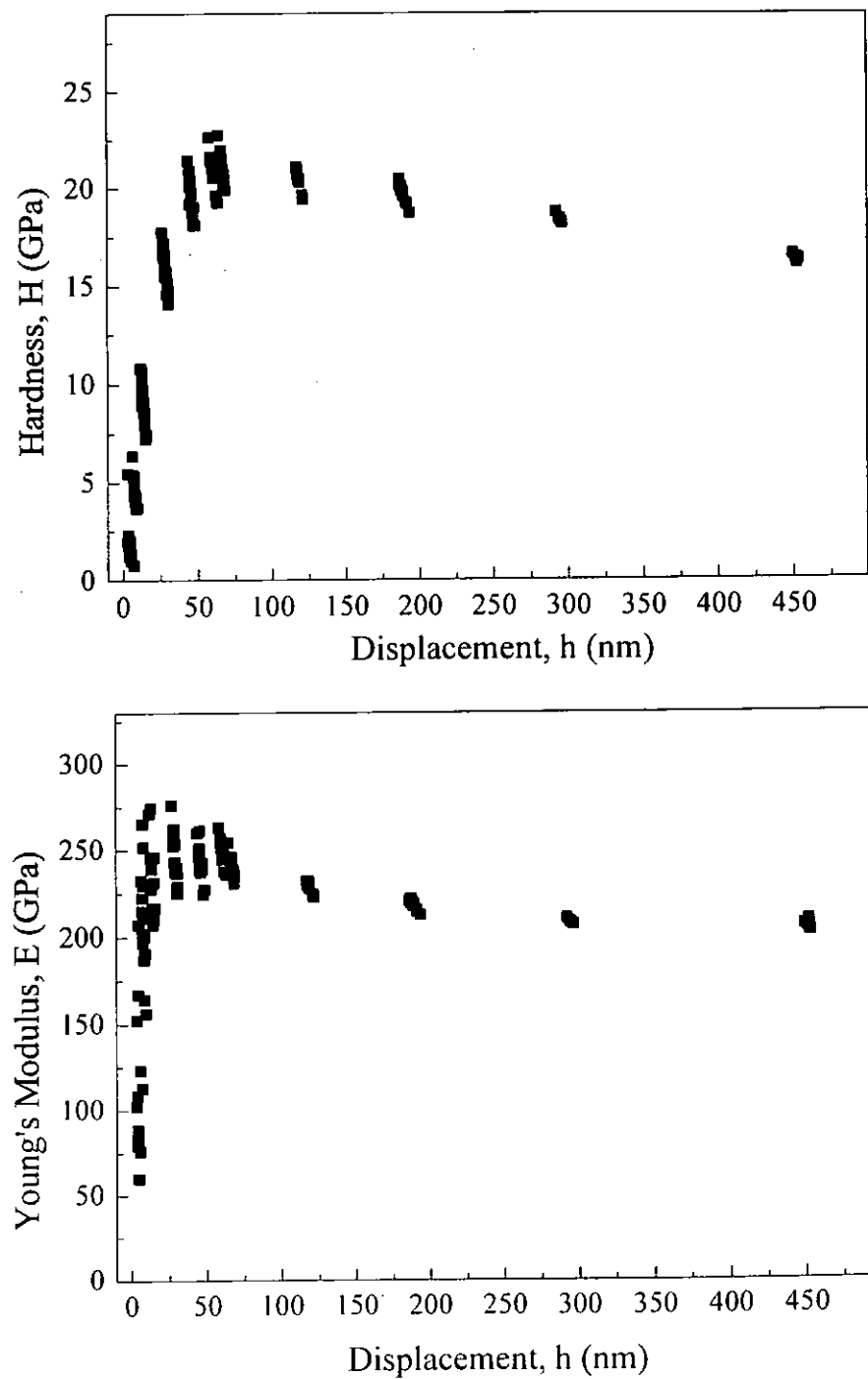


Fig. 4.12 Typical nanoindentation results hardness (H) and young's modulus (E) as functions of penetration depth.



4.3.2 Microstructure dependence of H and E of AlN films

Fig. 4.13 gives intuitive impressions on the difference for the load-unload curves of the AlN films having three different structures. In all the experiments, the maximum load was set at 3 mN. Fig. 4.13 (a), (b) and (c) show the load-unload curves of the films having the na-AlN, p-AlN and t-AlN structures, respectively. With this sequence, the maximum penetration depths were found to decrease from 80 nm, 66 nm and finally to 58 nm. In addition, the final depths of the indentation imprints (the end point of the unloading curves) also decrease from 40 nm, to 30 nm and then to 17 nm. Moreover, the work done of elastic recovery (area under the unloading curve) appears to have a larger fraction compared with the total work done (area under the unloading curve) when the film structure changes from na-AlN, to p-AlN and t-AlN.

All these features confirm that the hardness and young's modulus of a na-AlN film should be the smallest. The second should be those of a p-AlN film, and those of a t-AlN film should be the largest. Moreover, the na-AlN deformed more "plastically" during indentation, while the p-AlN and t-AlN films appear to be more elastic.

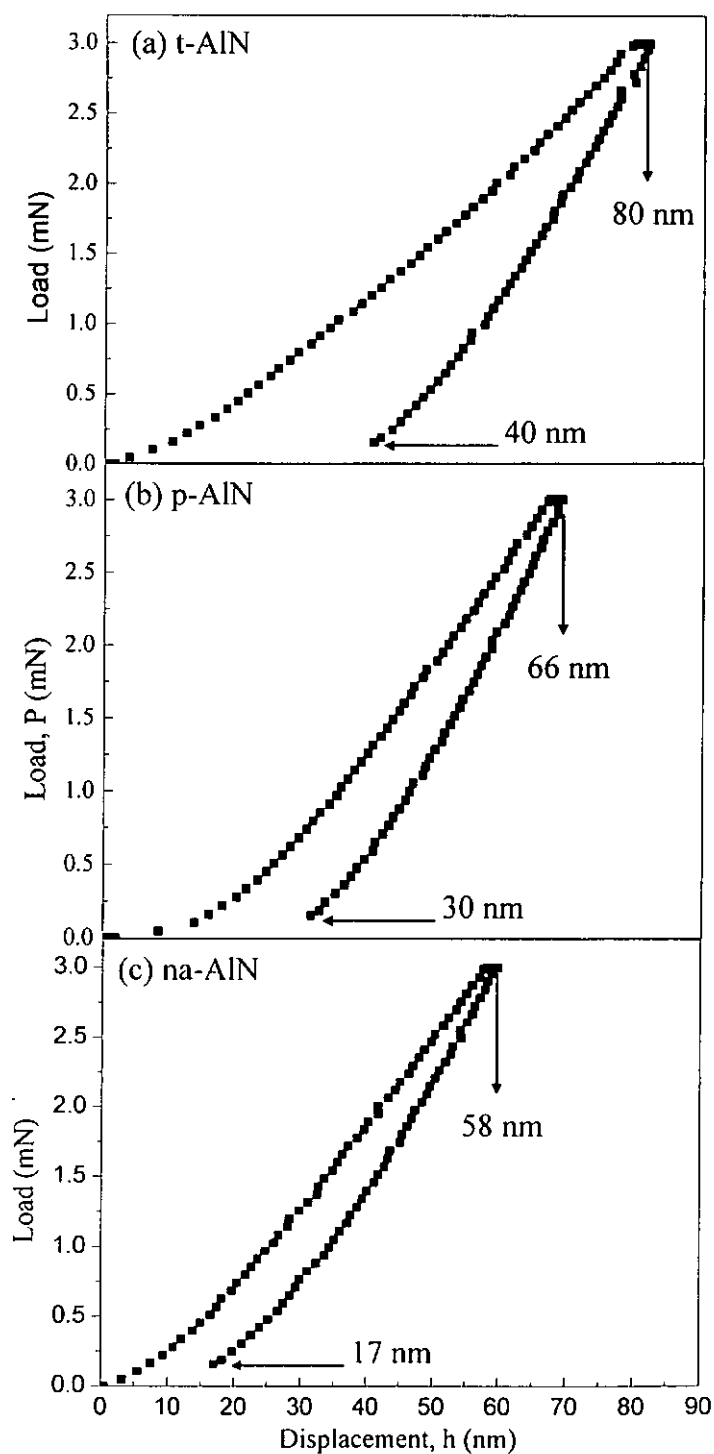


Fig. 4.13 The load-unload curve of AlN films with the structure of (a) nearly amorphous, (b) polycrystalline and (c) texture.



Fig. 4.14 shows the results of hardness and young's modulus of AlN films with different film structures. The data are tabulated in Table. 4.14. All of the results are recorded at depths around 1/10 of the film thickness. Obviously, difference in the film hardness is mainly due to the difference in the film structure. The t-AlN film is found to have the highest hardness of 18.8 - 20.9 GPa. The next is the p-AlN films, which hardness is in the range of 12.2 – 15.9 GPa. The na-AlN films show the lowest hardness of 12 GPa. This trend is explained considering that a film with a higher degree of crystallinity exhibits a denser structure. According to Rawdanowicz *et al* [Rawdanowicz, 1999] for example, the film could give a higher hardness.

Edgar *et al* [Edgar, 1996] reported that the hardness of their AlN film deposited by ion-beam-assisted deposition method was 23.7 GPa, which was higher than 20.9 GPa of the maximum value of our films. This is possibly due to the difference in the composition or impurity content of the AlN films prepared by the two different groups.



The trend of E is very similar to that of H , namely, it drops when the film structure is more disordered. For the t-AlN films, the values of E lie between 245 – 250 GPa. The values of E of the p-AlN films fall in the range of 220 – 242 GPa. E of the na-AlN films is the lowest, namely around 170 – 200 GPa. These results, therefore, imply strongly that the value of E of an AlN film is larger if the film has a higher degree of crystallization.

Film structure	Hardness (H)	Young's Modulus (E)
t-AlN	20.9 GPa	248.9 GPa
t-AlN	18.8 GPa	245.7 GPa
p-AlN	15.9 GPa	241.8 GPa
p-AlN	12.2 GPa	222.0 GPa
na-AlN	12.1 GPa	199.8 GPa
na-AlN	12.0 GPa	171.9 GPa

Table 4.14 Hardness and young's modulus of AlN films having different film structures.

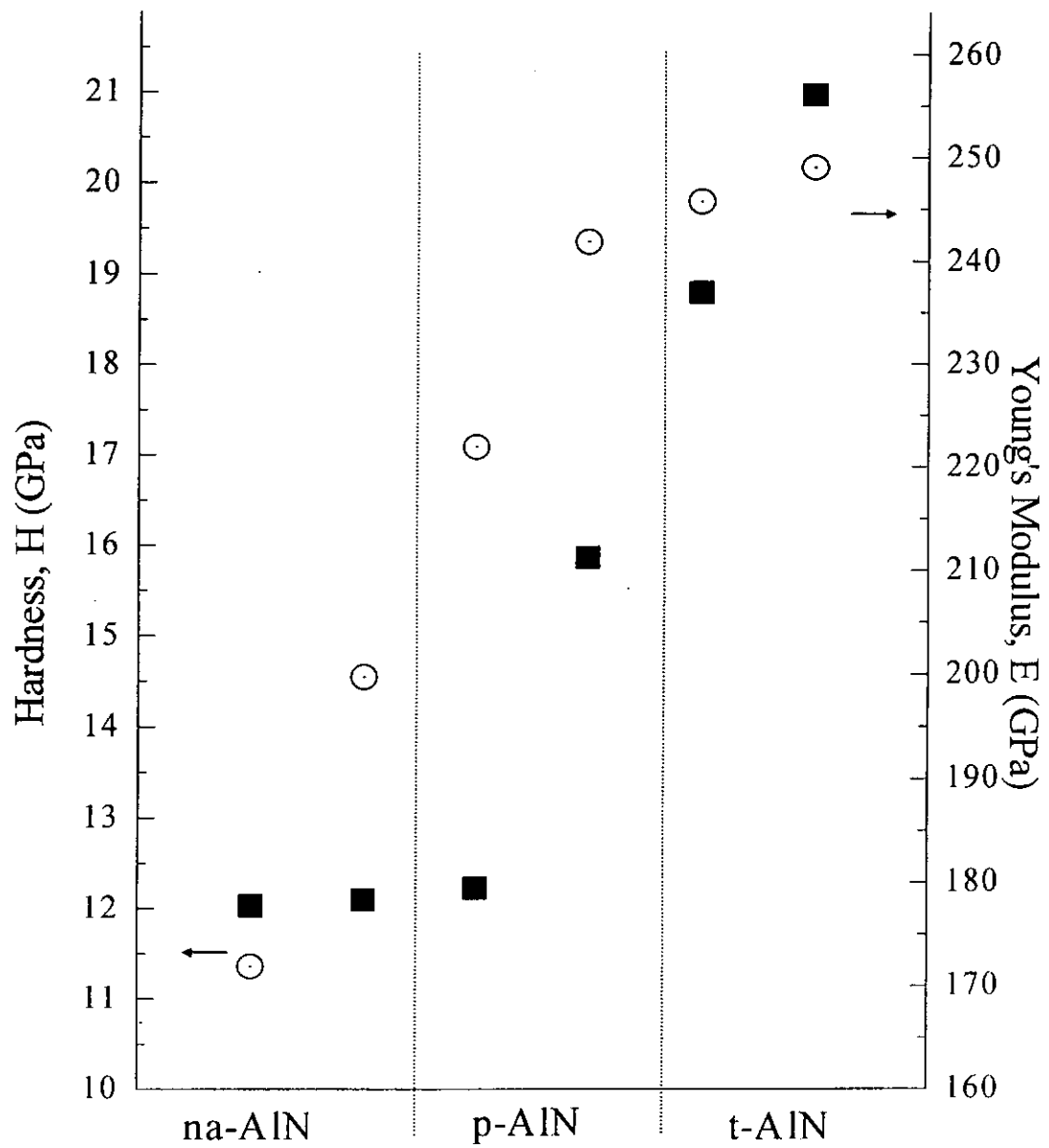


Fig. 4.14 Hardness (H) and young's modulus (E) of AlN films having different film structures.



Chapter 5

Conclusions

In this study, aluminum nitride (AlN) thin films of different crystallographic structures were fabricated by using radio-frequency reactive magnetron sputtering technique. Four different film structures can be identified. They are the nearly amorphous (na-) AlN, polycrystalline (p-) AlN, texture (t-) AlN and epitaxial (e-) AlN structures.

The formation of the above structures depends on the settings of several preparation parameters, including the substrate temperature T_s , (from room temperature to 700°C), power fed to the target P_w (from 100 W to 250 W), and the selection of substrate materials (Si(100), Pt(111)/Si(100) and $\text{Al}_2\text{O}_3(00\cdot1)$). Other parameters, such as target-to-substrate distance (D), mean free path (λ) and Ar/ N_2 gas ratio were kept unchanged.

A na-AlN film structure is produced when either one of the parameters (T_s and P_w) is set at the low level, or both are low. A na-AN film is characteristic of having an XRD 2θ - θ scan spectrum showing no observable diffraction peak. However, the GIXD spectrum collected with a small glancing angle of 3° contains very broad and weak diffraction peaks of AlN structure, indicating that the film contains very small AlN crystallites and the overall film structure is highly disordered.



The settings of moderate levels of T_s and P_w lead to the formation of the p-AlN structure. A p-AlN film is characteristic of having XRD 2θ - θ scan spectrum showing the three (10·0), (00·2) and (10·1) AlN peaks. The features of the XRD data show the presence of AlN grains in the p-AlN film, while their orientations relatively random.

With further increase in T_s and P_w , the t-AlN structure or e-AlN structure was formed. The t-AlN structure was formed when either Si(100) or Pt(111)/Si(100) substrate was used. The e-AlN structure was formed only when Al_2O_3 (00·1) substrate was used. The 2θ - θ spectra of both t-AlN and e-AlN exhibit a single peak of AlN(00·2) plane. The structures of t-AlN (on Si or Si/Pt) and e-AlN (on Al_2O_3) are distinguished by referring to their pole figures and ϕ -scan patterns.

FTIR absorption spectra reveal more details of the structures. The IR spectrum of a na-AlN film shows a broad absorption band covering the positions of many absorption bands of crystalline AlN. This feature confirms that the na-AlN structure is highly disordered, but may retain short range order of the crystalline AlN structure. The IR absorption band of a p-AlN film shows a main absorption band from the transverse $E_1(\text{TO})$ mode and a shoulder due to the $A_1(\text{TO})$ mode of AlN. They appear at 673 cm^{-1} and 610 cm^{-1} , respectively. The $E_1(\text{TO})$ mode and $A_1(\text{TO})$ mode vibrations were excited by the incident IR radiation interacting with the grains having the c-axis aligned in perpendicular and parallel to the substrate surface, respectively. The IR spectrum of a t-AlN film shows mainly the peak of the $E_1(\text{TO})$ mode at 673



cm^{-1} . This confirms that the grains in t-AlN film are aligned with their c-axis in perpendicular to the film surface.

A single beam laser interferometer was used to measure the piezoelectric coefficient d_{33} of the AlN films deposited on Pt(111)/Si(100) substrates. The value of d_{33} of the na-AlN film is the smallest, i.e. $\approx 0.2 \text{ pm V}^{-1}$. The d_{33} values of the p-AlN films lie in a rather broad region of $1.0 - 4.5 \text{ pm V}^{-1}$. Finally the value of d_{33} of the t-AlN films is 4.0 pm V^{-1} . The influence on the measurements of d_{33} due to the clamping effect by the substrate was found to be significant, and error of 30% can be induced if no correction is made in the calculation. The dielectric constant of the p-AlN films was measured in the frequency range of $10 \text{ kHz} - 1 \text{ MHz}$, and was determined to be $9 - 12.5$. For a high frequency range ($50 \text{ MHz} - 1 \text{ GHz}$) measurement, the capacitance was not recorded because of the influence of the resonance from internal circuit of the analyzer.

The hardnesses and young's moduli of the AlN films deposited on Si(100) substrates were measured by using the nanoindentation method. Results show that the hardness (H) and young's modulus (E) for the na-AlN films are the smallest ($H \approx 12 \text{ GPa}$ and $E \approx 170\text{-}190 \text{ GPa}$). H and E values of the p-AlN films are larger, i.e. $12 - 16 \text{ GPa}$ and $220 - 240 \text{ GPa}$, respectively. Those of the t-AlN films are the largest, i.e. $18 - 21 \text{ GPa}$ and 240 GPa , respectively. This reflects that higher H and E are accompanied by the denser film structure associated with the level of crystallization.



References

Assouar, M.B., Elmazria, O., Le Brizoual, L. and Alnot, P. "Reactive DC magnetron sputtering of aluminum nitride films for surface acoustic wave devices". *Diamond and Related Materials*, Vol. 11, pp.413-417 (2002)

Burianova, L., Sulc, M. and Prokopova, M. "Determination of the piezoelectric coefficients d_{ij} of PZT ceramics and composites by laser interferometry". *Journal of the European Ceramic Society*, Vol. 21, 1387-1390 (2001)

Cheng, C.C., Chen, Y.C., Horng, R.C., Wang, H.J., Chen, W.R. and Lai, E.K. "Growth of c-axis oriented aluminum nitride films on GaAs substrates by reactive rf magnetron sputtering". *Journal of Vacuum Science and Technology A*, Vol. 16, pp.3335-3340 (1998)

Cheng, C. C., Chen, Y. C., Wang, H. J. and Chen, W. R. "Low-temperature growth of aluminum nitride thin films on silicon by reactive radio frequency magnetron sputtering". *Journal of Vacuum Science and Technology A*, Vol. 14 (4), pp.2238-2242 (1996)

Cheng, H., Sun, Y. and Hing, P. "Microstructure evolution of AlN films deposited under various pressures by RF reactive sputtering". *Surface and Coatings Technology*, Vol. 166, pp.231-236 (2003)

Carlone, C., Lakin, K.M. and Shanks, H.R. "Optical phonons of aluminum nitride". *Journal of Applied Physics*, Vol. 55, pp.4010-4014 (1984)

Chubachi, Y., Sato, K. and Kojima, K. "Reflection high energy electron diffraction and X-ray studies of AlN films grown on Si(111) and Si(001) by organometallic chemical vapour deposition". *Thin Solid Films*, Vol. 122, pp.259-270 (1984)



- Cullity, B.D. and Stock, S.R., *Elements of X-Ray Diffraction*, p.388 (2001)
- Dubois, M.-A., Muralt, P. and Plessky, V. "BAW resonators based on AlN thin films". *IEEE Ultrasonics Symposium Proceedings 1999*, Vol. 2, pp.907-910 (1999)
- Edgar, J.H., Carosella, C.A., Eddy, C.R., Jr., and Smith, D.T. "Effect of beam voltage on the properties of aluminum nitride prepared by ion beam assisted deposition". *Journal of Material Science: Material in Electronics*, Vol. 7, p.247 (1996)
- Guy, I. L., Muensit, S. and Goldys, E. M. "Extensional piezoelectric coefficients of gallium nitride and aluminum nitride". *Applied Physics Letters*, Vol. 75, pp.4133-4135 (1999)
- Iriarte, G.F., Engelmark, F. and Katardjiev, I.V. "Reactive sputter deposition of highly orientated AlN films at room temperature". *Journal of Materials Research*, Vol. 17, pp.1469-1475 (2002)
- Ivanov, I., Hultman, L., Jarrendahl, K., Martensson, P. and Sundgren, J.-E. "Growth of epitaxial AlN (0001) on Si(111) by reactive magnetron sputter deposition". *Journal of Applied Physics*, Vol. 78 (9), pp.5721-5726 (1995)
- Jagannadham, K., Sharma, A. K., Wei, Q., Kalyanraman, R. and Naraan, J. "Structural characteristics of AlN films deposited by pulsed laser deposition and reactive magnetron sputtering: A comparative study". *Journal of Vacuum Science and Technology A*, Vol. 16 (5), pp.2804-2814 (1998)
- Kamiya, T. "Calculation of crystal structures, dielectric constants and piezoelectric properties of wurtzite-type crystals using ab-initio periodic Hartree-Fock method". *Japanese Journal of Applied Physics. Part 1*, Vol. 35, No. 8, pp.4421-4426 (1996)
- Kim, J.W. and Kim, H.K. "Low temperature epitaxial growth of AlN thin films on Al₂O₃(00·1) by reactive dc faced magnetron sputtering". *Journal of the Korean Physcial Society*, Vol. 32, pp.1664-1666 (1998)



Kobayashi, Y., Tanaka, N., Okano, H. Takeuchi, K., Usuki, T. and Shibata, K. "Characteristics of Surface Acoustic Wave on AlN Thin Films". *Japanese Journal of Applied Physics, Part 1*, Vol. 34, pp.2668-2673 (1995)

Kumar, A., Chan, H.L., Weimer, J.J. and Sanderson, L. "Structural characterization of pulsed laser-deposited AlN thin films on semiconductor substrates". *Thin Solid Films*, Vol. 308-309, pp.406-409 (1997)

Kung, P., Saxler, A., Zhang, X., Walker, D., Wang, T.C., Ferguson, I. and Razeghi, M. "High quality AlN and GaN epilayers grown on (00-1) sapphire, (100), and (111) silicon substrates". *Applied Physics Letters*, Vol. 66 (22), pp.2958-2960 (1995)

Kusaka, K., Taniguchi, D., Hanabusa, T. and Tominaga, K. "Effect of sputtering gas pressure and nitrogen concentration on crystal orientation and residual stress in sputtered AlN films". *Vacuum*, Vol. 66, pp.441-446 (2002)

Lakin, K.M., Kline, G.R. and McCarron, K.T. "Development of miniature filters for wireless applications". *IEEE Transaction on Microwave Theory and Techniques*, Vol. 43, pp.2933-2939 (1995)

Lee, H.C., Kim, G.H., Hong, S K., Lee, K.Y., Yong, Y.J., Chun, C.H. and Lee, J.Y. "Influence of sputtering pressure on the microstructure evolution of AlN thin films prepared by reactive sputtering". *Thin Solid Films*, Vol. 261, pp.148 – 153 (1995)

Lim, W.T., Son, B.K., Kang, D.H. and Lee, C.H. "Structural properties of AlN films grown on Si, Ru/Si and ZnO/Si substrates". *Thin Solid Films*, Vol. 382, pp.56-60 (2001)

Liu, J.M., Chong, N., Chan, H.L.W., Wong, K.H. and Choy, C.L. "Pulsed-laser-deposited epitaxial aluminum nitride films on (111) Si for surface acoustic-wave applications". *Applied Physics A*, Vol. 76, pp.93-96 (2003)



Loebl, H.P., Klee, M., Metzmacher, C., Brand, W. and Lok, P. "Piezoelectric thin AlN films for bulk acoustic wave (BAW) resonators". *Materials Chemistry and Physics*, Vol. 79, pp.143-146 (2003)

Lueng, C.M., Chan, H.L.W., Surya, C. and Choy, C. L. "Piezoelectric coefficient of aluminum nitride and gallium nitride". *Journal of Applied Physics*, Vol. 88, pp.5360-5363 (2000)

McNeil, L.E., Grimsditch, M. and French, R.H. "Vibrational spectroscopy of aluminum nitride". *Journal of the American Ceramic Society*, Vol. 76, p.1132 (1993)

National Bureau of Standards (U.S.) Monographs 25, Vol. 12, p.5 (1975)

Norton, M.G., Kotula, P.G. and Carter, C.B. "Oriented aluminum nitride thin films deposited by pulsed-laser ablation". *Journal of Applied Physics*, Vol. 70 (5), pp.2871-2873 (1991)

Nyquist, R.A. and Kagel, R.O. in *Infrared Spectra of Inorganic Compounds*, Academic Press, Orlando, p.209 (1971)

Okano, H., Takahashi, Y. and Tanaka, T. "Preparation of c-axis oriented AlN thin films by low-temperature reactive sputtering". *Japanese journal of Applied Physics. Part 1*, Vol. 31, pp.3446-3451 (1992)

Perlin, P., Polian, A. and Suski, T. "Raman-scattering studies of aluminum nitride at high pressure". *Physical Review B*, Vol. 57, No. 5, pp.2874-2877 (1993)

Rawdanowicz, T.A., Godbole, V., Narayan, J., Sankar, J. and Sharma, A. "The hardness and elastic moduli of pulsed laser deposited multiplayer AlN/TiN thin films". *Composites Part B*, Vol 30, pp.657-665 (1999)



- Rodriguez, B.J., Gruverman, A., Kingon, A. I. and Nemanich, R. J. "Piezoresponse force microscopy for piezoelectric measurements of III-nitride materials". *Journal of Crystal Growth*, Vol. 246, pp.252-258 (2002)
- Ruffner, J.A., Clem, P.G., Tuttle, B.A., Dimos, D. and Gonzales, D.M. "Effect of substrate composition on the piezoelectric response of reactively sputtered AlN thin films". *Thin Solid Films*, Vol. 354, pp.256-261 (1999)
- Ruiz, E. and Alvarez, S. "Electronic structure and properties of AlN". *Physics Review B*, Vol. 49, pp.7115-7123 (1994)
- Stevens, K.S., Ohtani, A., Kinniburgh, M. and Beresford, R. "Microstructure of AlN on Si (111) grown by plasma-assisted molecular beam epitaxy". *Applied Physics Letters*, Vol. 65 (3), pp.321-323 (1994)
- Sun, C.J., Kung, P., Saxler, A., Ohsato, H., Haritos, K. and Razeghi, M. "A crystallographic model of (00-1) aluminum nitride epitaxial thin film growth on (00-1) sapphire substrate". *Journal of Applied Physics*, Vol. 78 (8), pp.3964-3967 (1994)
- Tait, R.N. and Mirfazli, A. "Low temperature aluminum nitride deposition on aluminum by rf reactive sputtering". *Journal of Vacuum Science and Technology A*, Vol. 19 (4), pp.1586-1590 (2001)
- Vispute, R. D., Wu, H. and Jagannadham, K. "Epitaxial growth of AlN thin films on silicon (111) substrates by pulsed laser deposition". *Journal of Applied Physics*, Vol. 77 (9), pp.4724-4728 (1995)
- Watanabe, Y., Uchiyama, S., Nakamura, Y., Li, C.L., Sekino, T. and Niihara, K. "Mechanical properties and residual stress in AlN/Al mixed films prepared by ion-beam-assisted deposition". *Journal of Vacuum Science and Technology A*, Vol. 17 (2), pp.603-607 (1999)
- Wei, G. H. and Zi, J. "Zone-center optical phonons in wurtzite GaN and AlN". *Journal of Applied Physics*, Vol. 82 (9), pp.4693-4695 (1997)



Zhang, Q. M., Pan, W. Y. and Cross, L. E. "Laser interferometer for the study of piezoelectric and electrostrictive strain". *Journal of Applied Physics*, Vol. 63, pp.2492-2496 (1988)

Zhang, W., Vargas, R., Goto, T., Someno, Y. and Hirai, T. "Preparation of epitaxial AlN films by electron cyclotron resonance plasma-assisted chemical vapor deposition on Ir-and Pt-coated sapphire substrates". *Applied Physics Letter*, Vol. 64 (11), pp.1359-1361 (1994)